

## SUPPORTING INFORMATION

### Spatial Cross-Talk Between Oxidative Stress and DNA Replication in Human Fibroblasts

 Marko Radulovic,<sup>1,2</sup> Noor O Baqader,<sup>1</sup> Kai Stoeber,<sup>3†</sup> and Jasminka Godovac-Zimmermann<sup>1\*</sup>

<sup>1</sup>Division of Medicine, University College London, Center for Nephrology, Royal Free Campus, Rowland Hill Street, London, NW3 2PF, UK.

<sup>2</sup>Institute of Oncology and Radiology, Pasterova 14, 11000 Belgrade, Serbia

<sup>3</sup>Research Department of Pathology and UCL Cancer Institute, Rockefeller Building, University College London, University Street, London WC1E 6JJ, UK

<sup>†</sup>Present Address: Shionogi Europe, 33 Kingsway, Holborn, London WC2B 6UF, UK

## TABLE OF CONTENTS

### 1. Supplementary Figures 1-14 and Supplementary References.

Figure S-1. Network and joint spatial razor plot for 18 enzymes of glycolysis and the pentose phosphate shunt.

Figure S-2. Correlation of SILAC ratios between OXS and OAC for proteins assigned to the SAME class.

Figure S-3. Overlap matrix ( $r = 1$ ) for groups of CORUM complexes containing 19 proteins of the 49-set.

Figure S-4. Joint spatial razor plots for the Nop56p complex and FIB-associated complex involved in ribosome biogenesis.

Figure S-5. Analysis of the response of emerin nuclear envelope complexes to OXS and OAC.

Figure S-6. Joint spatial razor plots for the CCT protein folding complex, ATP synthase and V-Type ATPase.

Figure S-7. Joint spatial razor plots showing changes in subcellular abundance and compartmental distribution for proteins annotated by GO to nucleocytoplasmic transport (GO:0006913).

Figure S-8. Joint spatial razor plots showing changes in subcellular abundance and compartmental distribution for proteins annotated to endocytosis (GO:0006897).

Figure S-9. Joint spatial razor plots for 401-set proteins annotated by GO to small GTPase mediated signal transduction (GO:0007264) and/or GTPase activity (GO:0003924).

Figure S-10. Overlap matrix with radius = 2 and joint spatial razor plots for integrins, collagens and related proteins contained in the CORUM database.

Figure S-11. The overall set of 134,850 binary interaction pairs for the 4048-set of proteins.

Figure S-12. Interaction network for 401-set proteins clustered with the ClustNSee T-fit algorithm.

Figure S-13. Experimental weighted interaction network for the 401-set proteins for the clusters of the combined data set.

Figure S-14. The local STRING-based interaction networks for OXS/OAC around the proteins DNAJA1, GRPEL1, HSPA9 and TIMM44.

Supplementary References.

### 2. Supplementary Text. Methods used for selection of significant proteins.

### 3. Supplementary Tables

Supplementary Table 1. MS data for 4048-set of proteins.

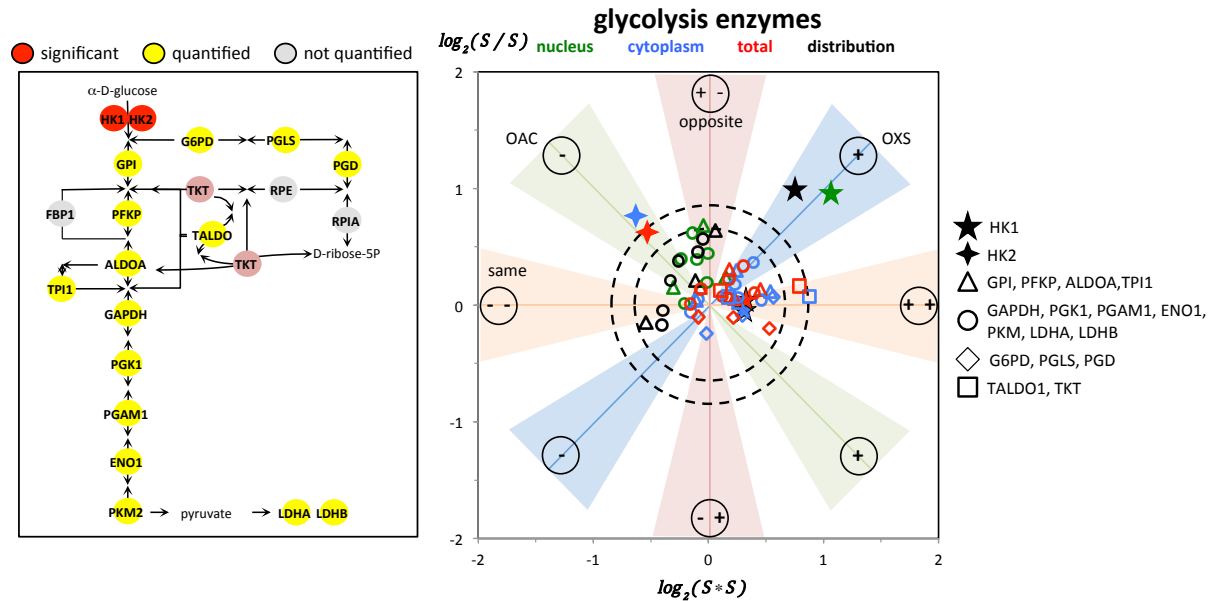
Supplementary Table 2. Summary of MS data for 401-set of significant proteins.

Supplementary Table 3. CORUM complexes for 401-set proteins.

Supplementary Table 4. Nuclear import-export annotation for 401-set proteins.

Supplementary Table 5. Vesicle trafficking annotation for 401-set proteins.

Supplementary Table 6. Binary interaction data for 401-set proteins.



Supplementary Figure 1. Network and joint spatial razor plot for 18 enzymes of glycolysis and the pentose phosphate shunt. The dominant changes are:

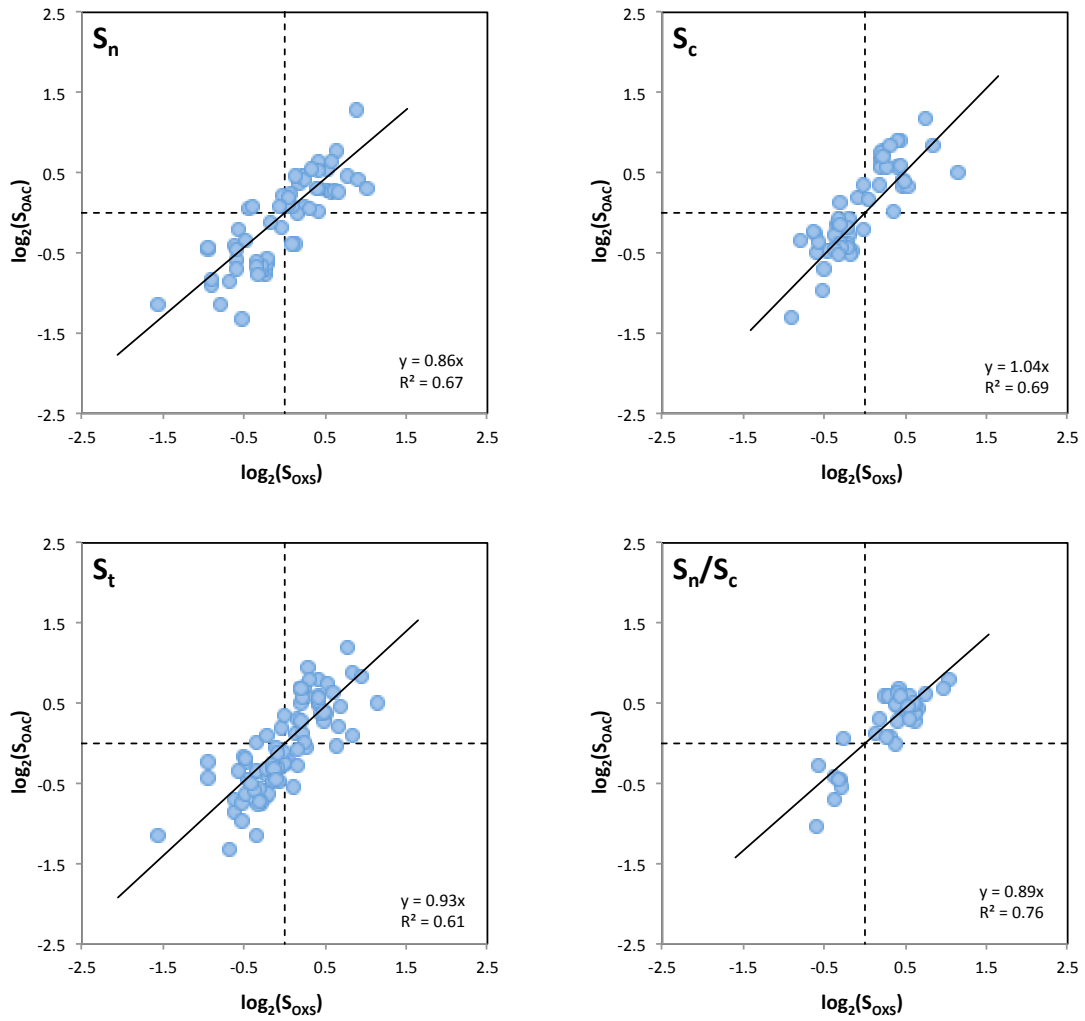
OXS: For HK1, increased nuclear abundance, C → N redistribution, little change in total or cytoplasmic abundance.

OAC: For HK2, decreased total and cytoplasmic abundance.

Both: For TKT, moderate increase in total and cytoplasmic abundance.

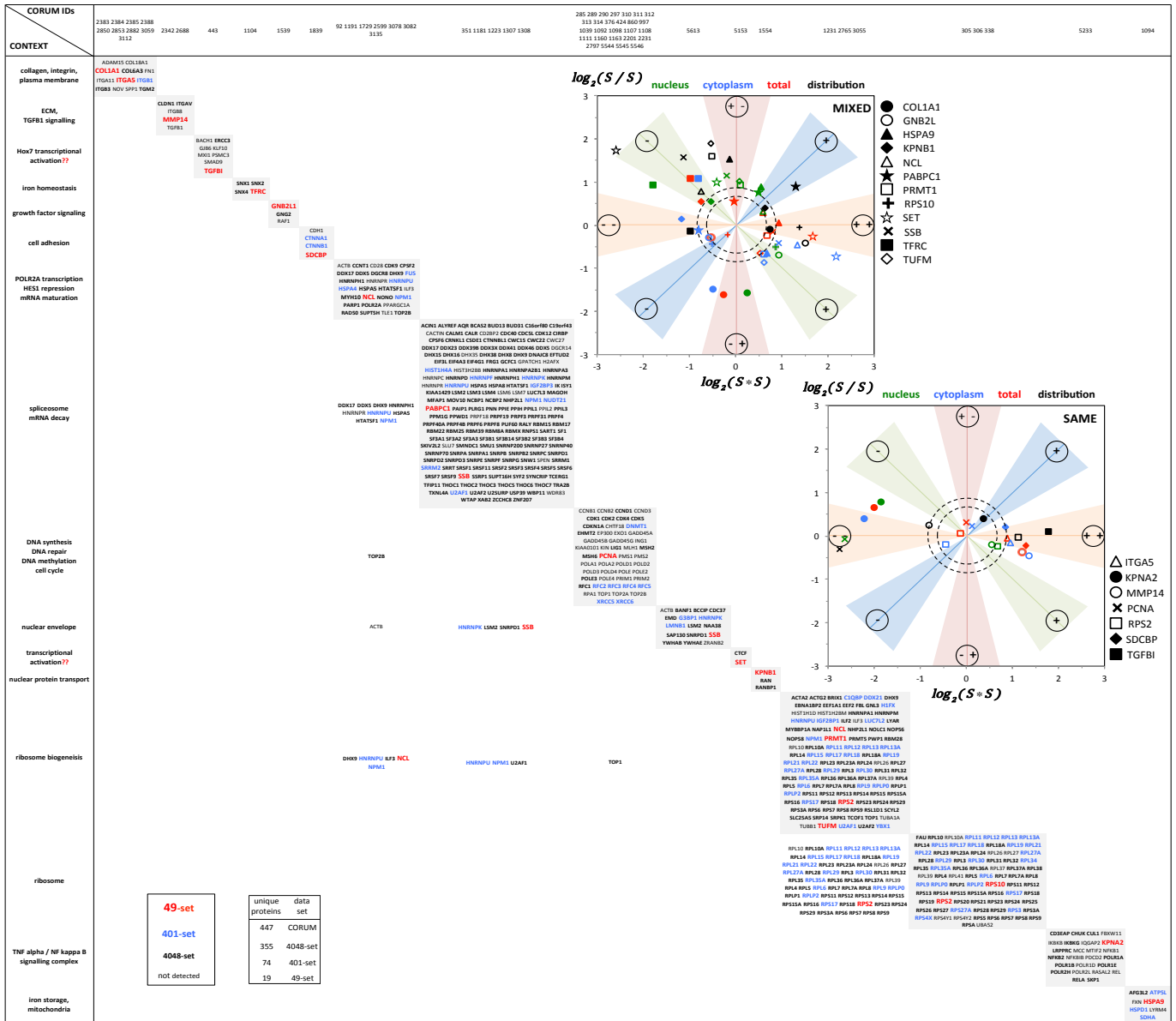
There are clear differences in the behaviour of HK1 and HK2 relative to OXS and OAC that may be related to their behavior in cancer cells. For example, HK2 is strongly overexpressed in many cancer cells. Recent work suggests that HK2 is required for the tumorigenicity of human non-small cell lung cancer and breast cancer cells, despite on-going expression of HK1 (Patra et al., 2013). In oncogenic KRas-induced non-small cell lung cancer cells, HK2 is required, in addition to HK1, for nucleotide biosynthesis via the non-oxidative pentose phosphate pathway, for the flow of citrate into the TCA cycle, and for glutamine utilization in the TCA cycle (Patra et al., 2013). Metabolomics studies indicated a decrease in the serine biosynthesis pathway and fatty acid synthesis in the absence of HK2 (Patra et al., 2013). The present results suggest that much of this may be a consequence of a proliferative state that can be interrupted by cell cycle arrest, e.g. OAC interruption of DNA replication substantially reduces HK2 total and cytoplasmic abundance. If so, the low expression of HK2 in most adult tissues, but high expression in cancer cells, may mainly be a reflection of proliferation/cell cycle status. In mammals, the effects of HK1/HK2 on metabolism have mostly been interpreted in terms of entry to glycolysis (above) and the interaction of HK1/HK2 with the mitochondrial outer membrane, with effects on both metabolism and apoptosis (Robey et al., 2005, 2006). In yeast the situation seems to be different. HXK2 is the predominant hexokinase in the presence of glucose, interaction with mitochondria apparently doesn't occur and HXK2 has (separable) functions both in input to glycolysis and, via phosphorylation-mediated nuclear import, transcriptional activities related to glucose repression and AMPK (Fernández-García, P. et al. (2012). In the absence of HXK2, HXK1 may substitute for HXK2 in some yeast strains (Kummel, A. et al., 2010). There is a little evidence for a similar nuclear role of HK2 in HeLa cells (Neary et al., 2010). We did not detect HK2 in the nucleus, but did detect a strong increase of HK1 nuclear abundance for OXS, which seemingly has not been previously described and is of unknown functional consequences. IMR90 fibroblasts are not cancer cells, but fibroblast metabolism can be important in the cancer microenvironment (Peiris-Pagès et al., 2015).

**References:** (See Supplementary References)

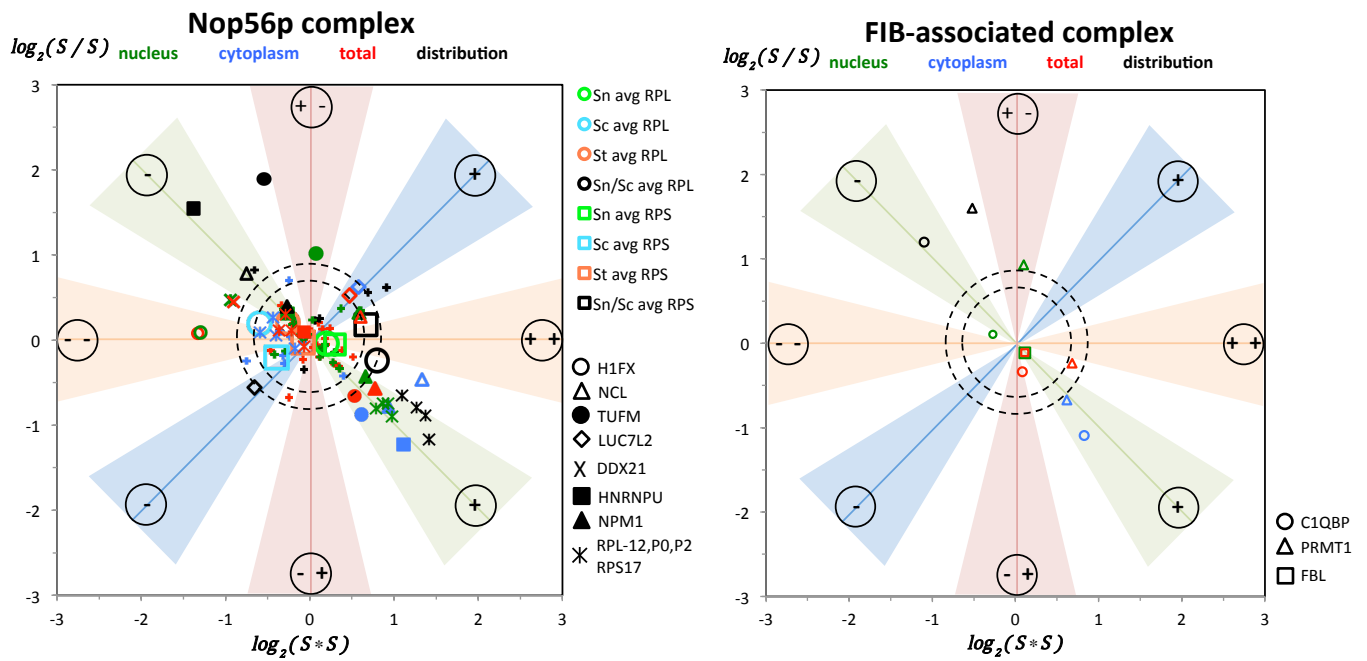


Supplementary Figure 2. Correlation of SILAC ratios between OXS and OAC for proteins assigned to the SAME class.

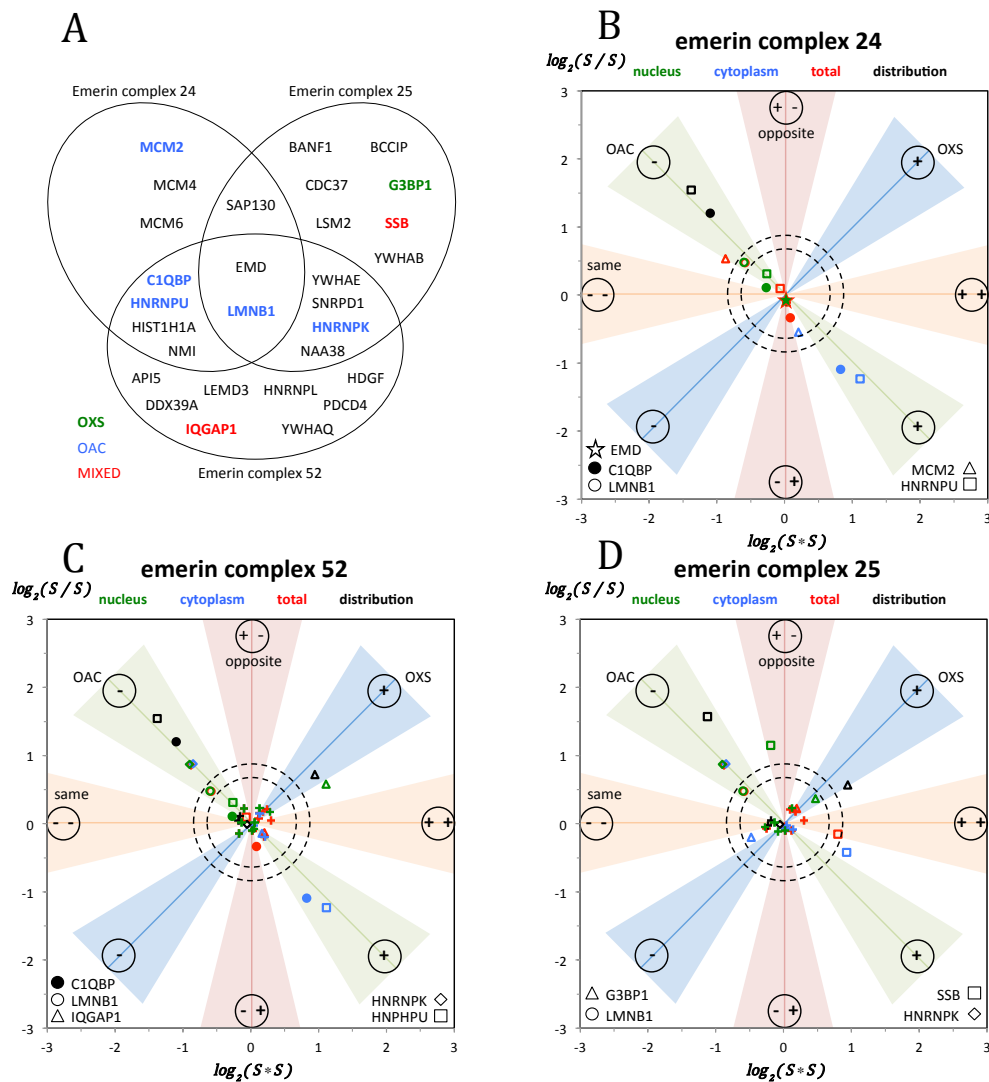
The relatively high correlations and the slopes of approximately one suggest that networks involving these proteins tend to show similar changes in abundance and distribution for both OXS and OAC.



Supplementary Figure 3. Overlap matrix ( $r = 1$ ) for groups of CORUM complexes containing 19 proteins of the 49-set. Scanning of all CORUM complexes identified 381 complexes (with 1176 unique proteins) that contained at least one 401-set protein. 196 proteins of the 401-set were included in at least one CORUM complex. 65 of the CORUM complexes (with 447 proteins) contained at least one protein of the experimental 49-set. The 4048-set detected 355 of the 447 proteins and 74 proteins were included in the 401-set. CORUM is partially redundant, i.e. some of the complexes were contained in other, larger complexes or were contained in groups of heavily overlapped complexes. Calculation of the overlap matrix for the 65 complexes led to condensation to the 16 groups of complexes shown. The diagonal elements of the overlap matrix show all proteins in the group. The proteins are encoded by their inclusion in the 49-set, the 401-set or the 4048-set according to the legend at lower left. Off-diagonal elements of the overlap matrix identify proteins that are shared between different groups. Apart from substantial overlap between the ribosome and ribosome biogenesis groups, there are very few proteins shared between the 16 different groups of complexes and each group contains at most a few proteins of the 49-set. This suggests that the 19 proteins of the 49-set dominate cross talk between OXS/OAC of the respective groups of proteins. Of the 19 proteins, 7 were classified as SAME and 12 as MIXED. The behaviour of the individual proteins is shown in the joint spatial razor plots inserted above the diagonal.

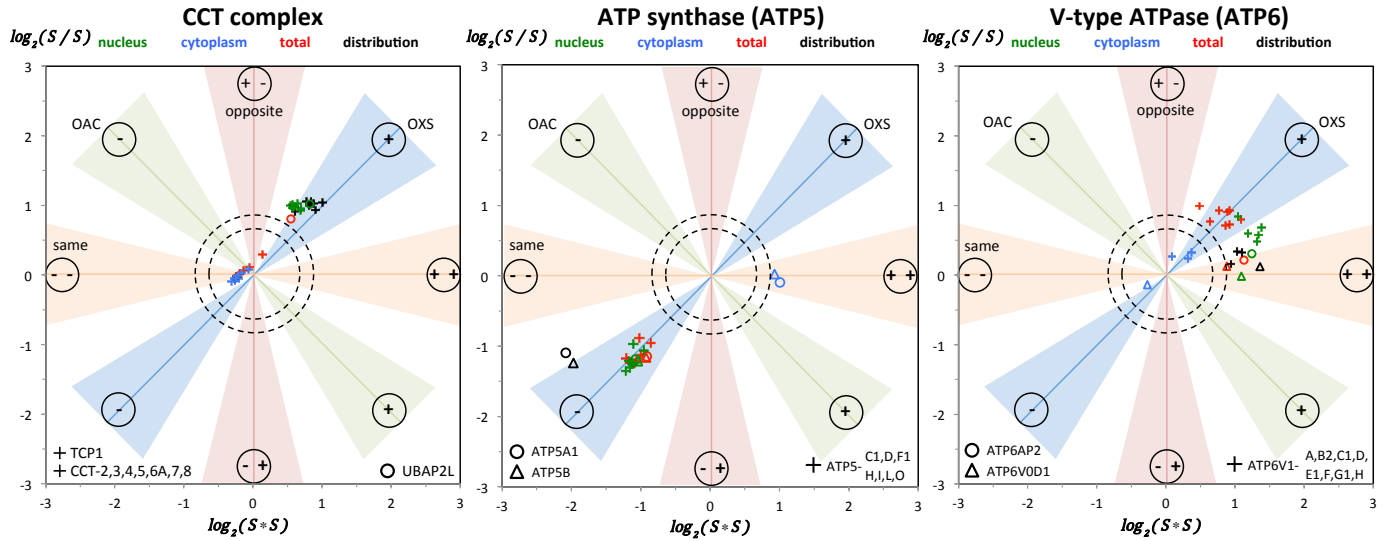


Supplementary Figure 4. Joint spatial razor plots for the Nop56p complex (104 proteins / 96 detected) and FIB-associated complex (6/4) involved in ribosome biogenesis. For the ribosomal proteins that did not show significant changes in compartmental abundance, average positions over the set of proteins are shown (see main text).



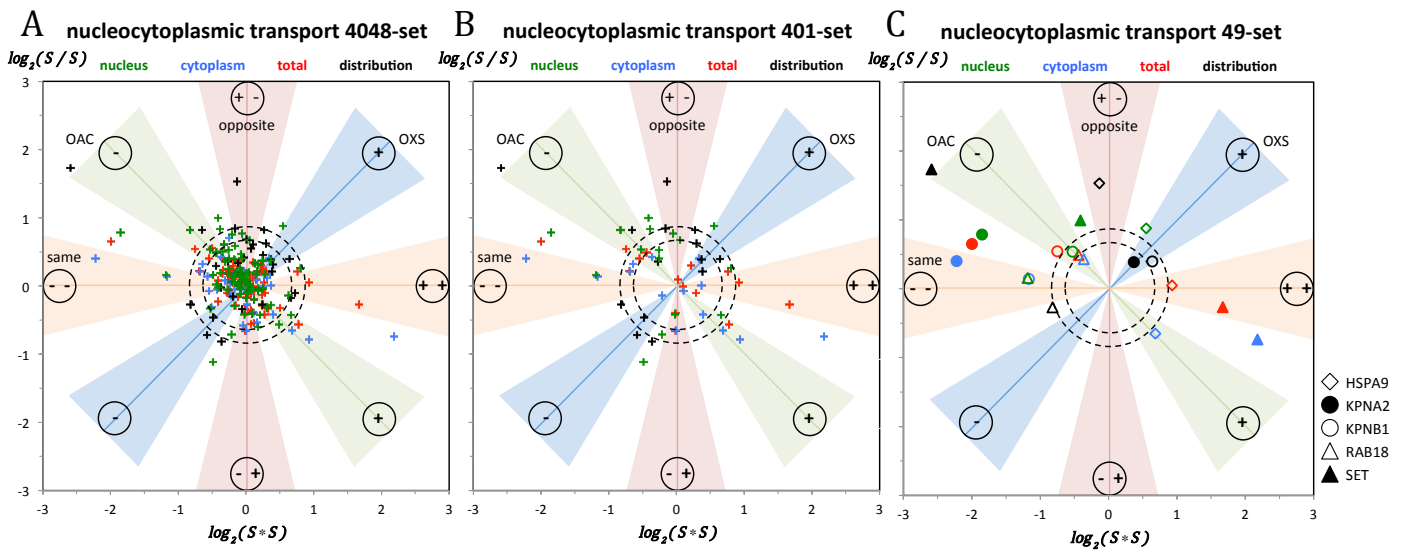
Supplementary Figure 5. Analysis of the response of emerlin nuclear envelope complexes to oxidative stress (OXS) and the DNA replication origin activation checkpoint (OAC). (A) Summary of the distribution of detected proteins over emerlin complexes 24, 25 and 52. Proteins with significant changes in SILAC ratios are shown in color. (B) – (D). Joint spatial razor plots for emerlin complexes 24, 52 and 25.

The nine Emerin complexes compiled in CORUM contain 59 different proteins, of which 44 were detected in our experiments. Significant changes were observed only for complexes containing lamin B1 (LMNB1). No apparent change was observed for Emerin (EMD, star in panel B). These two proteins are included in all three complexes with multiple changes, which have strongly intertwined protein content (panel A). Complex 24, which contains DNA replication licensing factors MCM2,4,6, appears to be mostly sensitive to OAC (panel B). Complex 52 appears to have modest crosstalk between OXS and OAC mediated by increased nuclear abundance of IQGAP1 (Ras GTPase-activating-like protein IQGAP1, panel C). Complex 25 has appreciable changes for OXS in nuclear/cytoplasmic distribution of G3BP1 (Ras GTPase-activating protein-binding protein 1) and substantial crosstalk between OXS and OAC mediated by opposing changes in the nuclear abundance of SSB (Lupus La protein, MIXED, panel D). The opposed changes in nuclear abundance of SSB result from a combination of increased total abundance (SAME) and redistribution between the nucleus and cytoplasm (OAC). For a given protein, its distribution over the different complexes and the functional consequences of changes in its abundance in each complex are under determined. Rebalancing over the abundance of the three complexes as a consequence of changes in total abundance and in compartmental distribution of individual proteins could result in functional intertwining.



Supplementary Figure 6. Joint spatial razor plots for the CCT protein folding complex, ATP synthase and V-Type ATPase.

The CCT protein folding complex shows strong C → N redistribution for OXS only that results in strong increase in nuclear abundance with little change in total or cytoplasmic abundance. Ubiquitin-associated protein 2-like (UBAP2L), which shows strong increase in total and nuclear abundance, is involved with the CCT complex in acrosomal membrane fusion processes. Nine different subunits of ATP synthase showed strongly reduced nuclear and total abundance for OXS only. Many subunits of the V1 subcomplex and 2 subunits of the V0 subcomplex of V-type ATPase show increased nuclear abundance for both OXS and OAC. This is achieved by C → N redistribution combined with increased total abundance for OXS and OAC (V0 subunits) or for OXS only (V1 subunits).

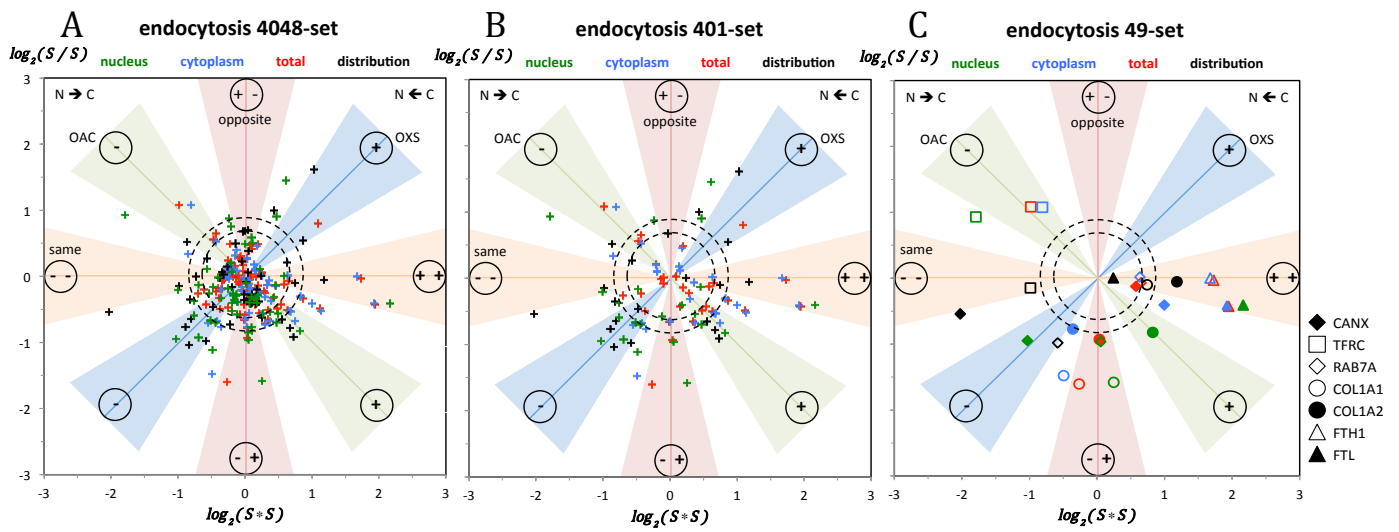


GO ID	GO process name	number proteins			gene IDs																				
		4048-set	401-set	49-set	401-set																				
GO:0006913	nucleocytoplasmic transport	197	16	5	CHP1	FYTTD1	G3BP2	HSPA9	IPOS	IPO7	KPNA2	KPNB1	NPM1	HSPA9	KPNA2	KPNB1	RAB18	RAB34	RANGAP1	SET	SPTBN1	U2AF1	XPO1	RAB18	SET

Supplementary Figure 7. Joint spatial razor plots showing changes in subcellular abundance and compartmental distribution for proteins annotated by GO to nucleocytoplasmic transport (GO:0006913). (A) 197 proteins detected in the 4048-set. (B) 16 proteins in the 401-set with at least one significant SILAC ratio pair in OXS or OAC. (C) 5 proteins in the 49-set with at least one SILAC ratio pair significant in both OXS and OAC.

Protein KPNA2 shows SAME behaviour between OAC and OXS consisting of substantial reduction in total, nuclear and cytoplasmic abundance with limited redistribution for OXS. KPNB1 (MIXED) shows trends similar to KPNA2 for total abundance and redistribution with a different balance that predominantly results in substantial reduction in cytoplasmic abundance for both OXS and OAC. SET (MIXED) shows strong increases in total and cytoplasmic abundance for OXS/OAC, accompanied by very strong N → C redistribution predominantly for OAC that results in a substantial decrease in nuclear abundance for OAC. HSPA9 (MIXED) shows strong increase in total abundance for OXS/OAC, but strongly opposite N ↔ C redistribution that results in strong increase in nuclear abundance for OXS and strong increase in cytoplasmic abundance for OAC

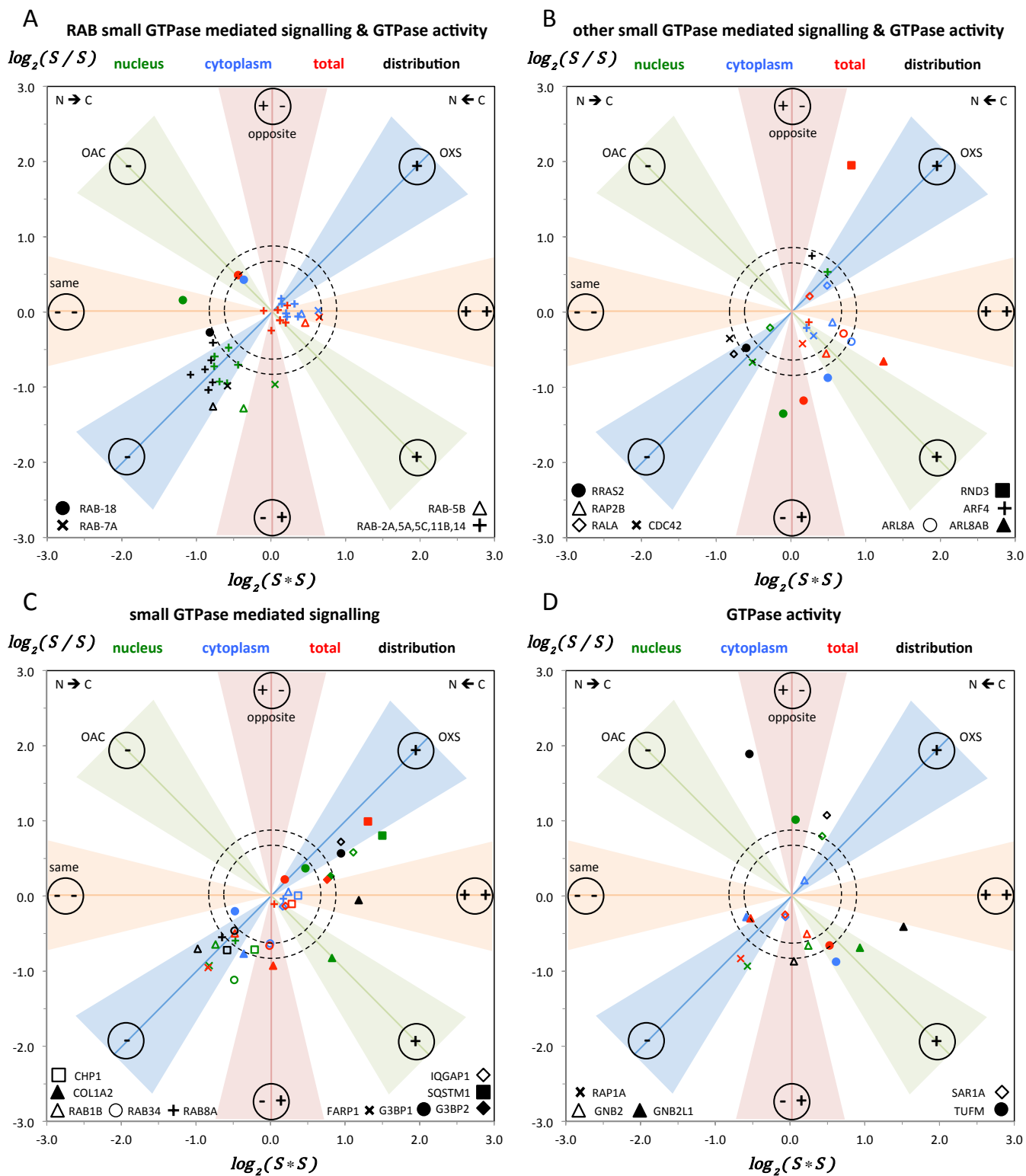




GO ID	GO process name	gene IDs																																						
		4048-set	401-set	49-set	401-set			49-set																																
GO:0006897	endocytosis	162	29	7	ANXA11	AP2A1	AP2B1	ATP6V1H	CANX	CAV1	CDC42	COL1A1	COL1A2	FTH1	FTL	HSP90AA1	HSPH1	IGF2R	KRAS	LRP1	LRPAP1	M6PR	MFG8	MRC2	NME1	PICALM	RAB14	RAB1A	RAB34	RAB5A	RAB7A	SPARC	TFRC	CANX	COL1A1	COL1A2	FTH1	FTL	RAB7A	TFRC

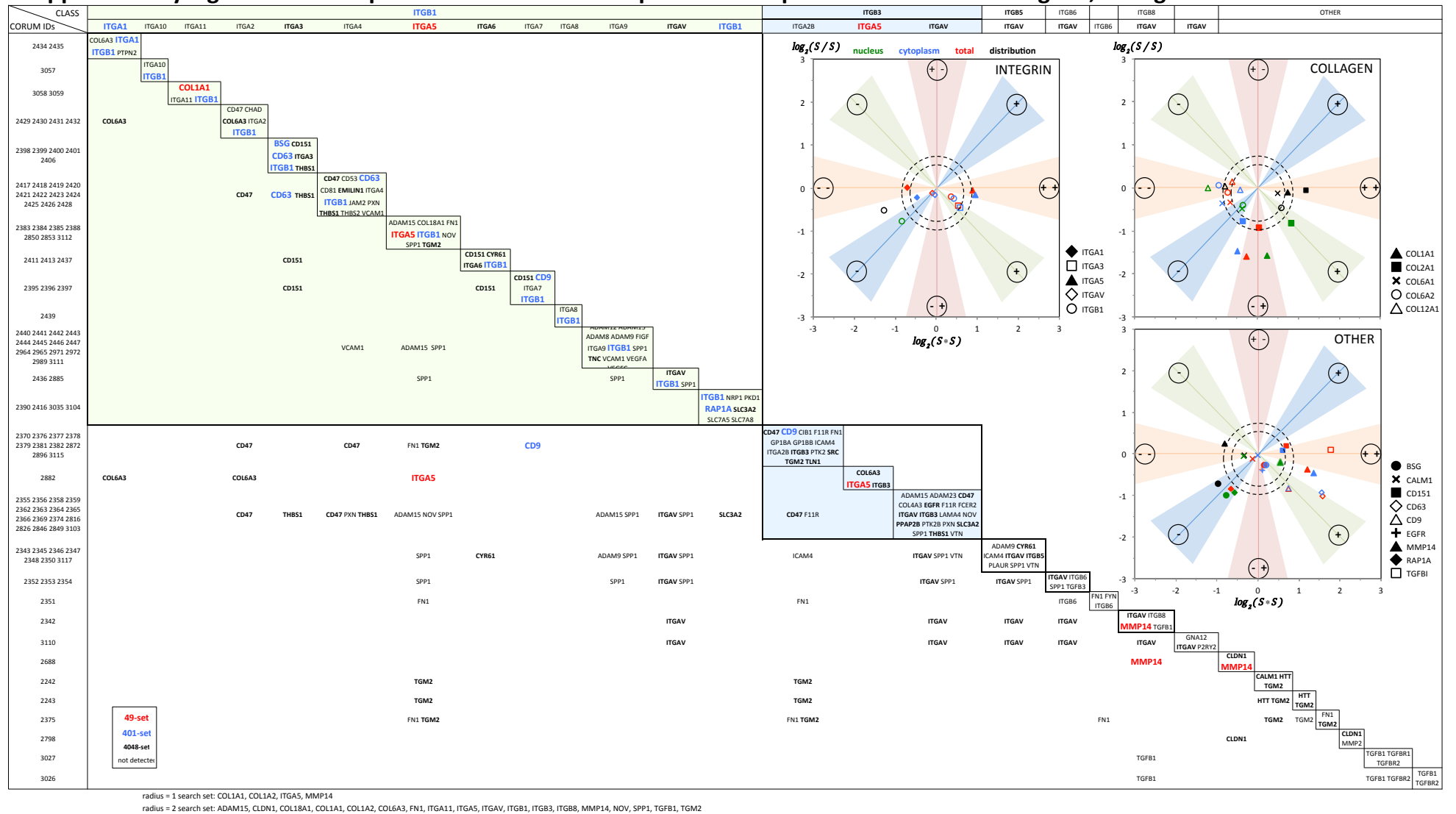
Supplementary Figure 8. Joint spatial razor plots showing changes in subcellular abundance and compartmental distribution for proteins annotated to endocytosis (GO:0006897). (A) 162 proteins detected in the 4048-set. (B) 29 proteins in the 401-set with at least one significant SILAC ratio pair in OXS or OAC. (C) 7 proteins in the 49-set with at least one SILAC ratio pair significant in both OXS and OAC.

Two proteins (FTH1, FTL) included in the 49-set show SAME behaviour: strong increase in total abundance with little or no redistribution. Although these two proteins are vesicle-bound, they appear to readily re-equilibrate between the nuclear/cytoplasmic compartments. The other five proteins show MIXED behaviour, which can be complex. For example, COL1A2 shows same, strong C → N redistribution for OXS/OAC, but substantial decrease/increase in total abundance for OXS/OAC. The dominant effect is then a substantial decrease in cytoplasmic abundance for OXS, but a substantial increase in nuclear abundance for OAC. COL1A1 shows similar trends for total abundance/redistribution, but with different balance between the two. This produces substantial decrease/increase in both nuclear/cytoplasmic compartment abundances for OXS/OAC. RAB7A shows same, modest increase in total abundance, but strong N → C redistribution predominantly for OXS. The dominant feature is a strong decrease/increase in nuclear abundance for OXS/OAC. Note that 3 of these proteins (TFRC, FTH1, FTL) are involved in iron homeostasis.



Supplementary Figure 9. Joint spatial razor plots for 401-set proteins annotated by GO to small GTPase mediated signal transduction (GO:0007264) and/or GTPase activity (GO:0003924). (A) Ras-related Rab proteins annotated to both identifiers. (B) Other proteins annotated to both identifiers. (C) Proteins annotated to small GTPase mediated signal transduction. (D) Proteins annotated to GTPase activity.

## Supplementary Figure 10. Overlap Matrix for CORUM Complexes and Experimental Data for Integrins, Collagens and Related Proteins



Supplementary Figure 10. Overlap matrix with radius = 2 for integrins, collagens and related proteins contained in the CORUM database. The CORUM database was scanned for complexes containing one or more of the 49-set proteins COL1A1, COL1A2, ITGA5 and MMP14 (radius = 1). This identified a set of 11 independent complexes. The 17 proteins contained in these complexes were then used as an augmented search set (radius = 2) to identify further complexes. The radius = 2 search identified 106 partially redundant complexes containing 90 unique proteins. Complexes containing integrin components of type ITGA and ITGB were then grouped according to the ITGA/ITGB combination. CORUM also contained complexes of OTHER proteins for (ITGB1/ITGB6 without ITGA) and (ITGAV without ITGB), which are listed in separate columns. Some of the OTHER proteins were also contained in complexes without ITGA or ITGB, which are listed in the OTHER columns. Proteins that were contained in more than one type of ITGA/ITGB or OTHER complex are indicated by the (lower) off-diagonal elements. In the green (ITGB1) and blue (ITGB3) regions, off-diagonal repetitions of ITGB1 and ITGB3 were omitted to improve visualization of OTHER proteins. Proteins detected experimentally are classified according to their inclusion in the 4048-set, 401-set or 49-set according to the legend (lower left). The joint spatial razor plot inserts in the upper off-diagonal region show the experimental behaviour of the 401-set, 49-set and selected other proteins.

**Overall, the substantial changes observed for both OXS/OAC for proteins involved in plasma membrane/ECM processes suggest complex, interrelated networks involving the plasma membrane, the extracellular matrix and the nucleus.** Although the CORUM complexes certainly represent an incomplete sampling of ECM processes, the present results (see below) provide overwhelming evidence that there are strong interconnections between the nucleus and the plasma membrane/extracellular matrix, even for a nominally nuclear-centered process such as OAC. Many of these interconnections also involve proteins related to OXS. Notable is that many of the same proteins are widely investigated for their putative relationships to disease processes, especially cancer. The present results suggest that many of the changes/functions are inherent to both proliferation and oxidative state in normal cells and that better understanding of the functional networks in normal cells would aid enormously in identifying changes crucial to disease processes. Although it is still technically challenging, non-biased monitoring of concurrent changes in the abundance, form and subcellular distribution of whole networks that may involve hundreds of proteins, rather than a few selected proteins, seems to be required.

**Distinctive changes in ITGA/ITGB pairs and collagens in both the nucleus and cytoplasm are observed for OXS/OAC.** Among the family of integrins (Barczyk et al., 2010), we monitored pairs that bind to collagens ( $\alpha1\beta1$ ), laminins ( $\alpha3\beta1$ ) and fibronectin/vitronectin ( $\alpha5\beta1$ ;  $\alpha v\beta1$ ) with large numbers of SILAC ratio counts. ITGA1, ITGA3 and ITGA5 showed various changes in total/cytoplasmic abundance for OAC/OXS. No change was detected for ITGAV. There were increases in the ITGA3/ITGA5 vs. ITGA1 ratio (laminin-fibronectin vs. collagen binding) for both OXS/OAC. For ITGB1, there was a strong decrease in nuclear abundance for OXS. For

collagens COL6A1, COL6A2 and COL12A1 there were generally moderate decreases in abundance for OXS/OAC. For OAC, COL1A1 and COL1A2 showed strong increase in total and nuclear/cytoplasmic abundance, with C  $\rightarrow$  N redistribution resulting in the strongest changes in the nucleus. For OXS, COL1A1 and COL1A2 showed strong decrease in total/cytoplasmic abundance, but only COL1A1 decreased strongly in nuclear abundance. These decreases in cytoplasmic abundance parallel the decrease in ITGA1, suggesting re-balancing of collagen binding vs. laminin/fibronectin binding may be strongest for OXS. The distinctive changes detected for collagens such as COL1A1 are unanticipated, but are not entirely surprising. The trafficking of collagen to the ECM requires very elaborate post-translational processing to stabilize and target the collagen triple helix to the ECM. Without such processing, the collagen triple helix is unstable. A key step is hydroxylation of proline, for which ferrous ions,  $\alpha$ -ketoglutarate, oxygen and ascorbic acid are all cofactors. That is, intimate connections to the oxidative state of cells and perhaps to TCA metabolism and iron homeostasis are implicit. We see extensive changes for the TCA cycle and iron/heme proteins (Baqader et al, 2014). Our set of significant proteins includes proline 4-hydroxylase and also proline 3-hydroxylases-1,3, whose changes in nuclear abundance seem to parallel COL1A1. Glycosylation of collagens is also crucial and we also see changes in Procollagen galactosyltransferase 1 as well as several other glycosyltransferases of the endoplasmic reticulum. Studies of osteoblasts indicate that procollagen trafficking can be linked to cytoplasmic vesicles and RAB proteins such as RAB1, RAB3D and RAB27b (Nabavi et al, 2012). RAB1A is included in our set of significant proteins.

**A strong decrease of total and nuclear abundance of the small GTPase Rap1a for OXS** is a distinctive change. Rap1a plays a crucial role in cell adhesion, migration and polarity. It cycles

between the cytoplasm and the plasma membrane (Takahashi et al., 2013) and also locates to the perinuclear region (Wang et al., 2006). It is intimately involved in control of cell junctions through regulation of actin cytoskeletal dynamics (Ando et al., 2013, Post et al., 2015). Integrin activation can be controlled by Rap1a (Ahmed et al., 2010) and may involve microtubule transport since KIF14 negatively regulates Rap1a-Radil signalling and integrin activation during breast cancer progression (Ahmed et al., 2012). Rap1a has recently been linked to cell migration via TNFB induced ROS signalling involving NADPH Oxidase and NFkB-dependent activation of Rac1 (Wang et al., 2015). Our results suggest that the many activities of Rap1a may be tied to the cell cycle/oxidative state of cells and that nuclear Rap1a may influence these states. A further connection to metabolic/oxidative state is the importance of cAMP to Rap1a activity (Wang et al., 2006) and the cAMP-dependent protein kinase type I-alpha regulatory subunit (PRKAR1A) is also included in the 401-set of proteins with significant changes (Supplementary Table 2).

**Basigin shows strongly reduced nuclear abundance for OXS.** Basigin (BSG, also known as CDC147, HAb18G and EMMPRIN) is a trans-membrane protein of the integrin superfamily with two C2-type immunoglobulin domains in the extracellular N-terminal sequence. It has been associated with a variety of diseases, including many types of cancer (Weidle et al., 2010, Xiong et al., 2014). Its functional activities include: (1) promotion of tumour invasion and metastasis by induced expression of matrix metalloproteinases in cancer and stromal cells (Weidle et al., 2010, Xiong et al., 2014); (2) induction of invadopodia-like structures containing MMP14 in non-cancerous epithelial cells (Grass et al., 2012); (3) interaction with integrins  $\alpha3\beta1$  (Tang et al., 2008) and  $\alpha6\beta1$  (Dai et al., 2009) as well as caveolin (Tang and Hemler, 2004); and, (4) complex

formation with the MCT1/MCT4 lactate symporters that are critical to energetics and growth of glycolytic tumors (Kirk et al., 2000, Le Floch et al., 2011). We observed strong decrease in the nuclear abundance of BSG for OXS as a consequence of N → C redistribution with little change in total/cytoplasmic abundance. The influence of oxidative stress on BSG function seems to have been little investigated apart from reports of the inducible expression of BSG (Ke et al., 2012) and MCT4 (Ullah et al., 2006) by HIF1 under hypoxic conditions. Functions associated with nuclear effects of BSG have also received only very limited attention (Weidle et al., 2010, Xiong et al., 2014). BSG in the vesicular exosome enhances tumour cell proliferation (Arendt et al., 2014) and vesicular trafficking of MMP14 recently has been associated with various RAB small GTPases (Linder and Scita, 2015). The present results suggest that the nuclear transfer of BSG may be related to SNARE-based vesicle trafficking and RABs (see below).

**Numerous proteins involved in Transforming Growth Factor  $\beta$  pathways are changed.** We monitored 196 proteins for which STRING contains interactions (medium confidence, combined score > 400) to TGF $\beta$  (TGFB1,2,3) or their receptor (TGFB1,2). Supplementary Table 2 shows the data for 33 proteins contained in the 401-set (preselected groups, filter = TGFB). Clear evidence for involvement of networks related to TGFB is the strong SAME increase in total/nuclear abundance for OAC/OXS observed for Transforming growth factor-beta-induced protein ig-h3 (TGFBI, also known as  $\beta$ ig-H3). With small numbers of ratio counts, similar increases were observed in the cytoplasmic compartment (Supplementary Table 2). TGFBI has been characterized as a secreted ECM protein that can interact with collagens, proteoglycans and various integrins including  $\alpha$ 3 $\beta$ 1 (Kim et al., 2000),  $\alpha$ 2 $\beta$ 1 (Guo et al., 2014) and  $\alpha$ v $\beta$ 3 (Choi et al., 2015), can be internalized via caveolae-mediated endocytosis (Choi et al., 2015), and is involved in a number of diseases, including various cancers (Ween et al., 2012, Han et al., 2015). It has previously been reported in the nucleus (Billings et al., 2000), but this has been little further investigated. In keeping with upregulation of TGFBI and connections of TGF-beta to ECM remodelling, a variety of other ECM proteins that have STRING interactions with TGFB/TGFB1 are in the 401-set: CAV1, COL1A1, COL1A2, COL6A1, CTNNA1, ITGA5, ITGB1, MMP14, SERPINE1, SPARC, TAGLN and TIMP1 (Supplementary Table 2, filter: preselected groups = TGFB). However, numerous other proteins (ANXA2, AP2B1, CDC42, CSRP2, F3, HADHB, HMGA2, HMOX1, IQGAP1, KRAS, LAMB1, LRP1, PCNA, PRKAR1A, RPS27A, SAR1A, SPTBN1, TRAP1, YBX1), including even nuclear export proteins (XPO1), are also included and many of these proteins show substantial nuclear changes. This emphasizes strong and intricate intertwining between nuclear and ECM processes for OAC/OXS.

**Matrix metalloproteinase 14 shows substantially increased total and cytoplasmic abundance for OAC.** The best-characterized functions of MMP14 (also known as MT1-MMP) are in remodelling the ECM via proteolysis of numerous ECM proteins, including collagens, as well as activation of other metalloproteinases such as MMP2 and MMP13 (Zucker et al., 2003, Kessenbrock et al., 2010, Gingras and Beliveau, 2010, Rodriguez et al., 2010). Shedding of MMP14-containing microvesicles by processes involving proteins such as the v-SNARE VAMP3 and tetraspanin CD9 can promote tumour invasion (Clancy et al., 2015) and MMP14 may also be involved in stromal fibroblast remodelling that facilitates cancer cell invasion by invadopodia-independent matrix degradation processes (Cao et al., 2015). However, in addition

to proteolytic remodelling of ECM components, there is increasing evidence that MMP14 is also involved in other intracellular signalling systems that include non-proteolytic activation of AKT/ERK1,2 signalling (Valacca et al., 2015) as well as NF- $\kappa$ B-mediated cyclooxygenase-2 (PTSG2) expression, fibroblast growth factor-2 (FGF2) signalling, and activation of the YAP and TAZ transcriptional coactivators (see Refs in Valacca et al., 2015). A novel non-membrane activity is localization to centrosomes of dividing cells, where MMP14 cleaves pericentrin-2 (Strongin, 2006). MMP14 is implicated in the breaching of basement membranes by tumour cells, in cell invasion through interstitial collagen tissues and it accumulates at invadopodia. It is subject endocytosis by clathrin- and caveolae-dependent pathways and recycled back to the plasma membrane via recycling endosomes or the post trans-Golgi network (Poincloux et al., 2009).

**Vesicle-mediated trafficking with the nucleus may be involved.** For both OXS/OAC, changes involving N → C redistribution result in larger increases for cytoplasmic than nuclear abundance for MMP14. There is evidence for vesicle-mediated trafficking involving SNAREs for matrix metalloproteinase secretion and for MMP14 localization and cell invasion (Miyata et al., 2004; Steffen et al., 2008; Kean et al., 2009; Williams and Coppolino, 2011, Williams et al. 2014). This has been previously associated with Synaptosomal-associated protein 23 (SNAP23), Vesicle-associated membrane protein 7 (VAMP7), and syntaxin 4 (STX4) (Williams et al., 2014) or with SNAP23, VAMP3, and STX12 (Kean et al., 2009). Recently SNAP23, VAMP3, and STX12 have been associated with the transfer of SRC, EGFR, and ITGB1 from a RAB-11 enriched perinuclear compartment to invadopodia of MDA-MB-231 and HT1080 cancer cells (Williams and Coppolino, 2014).

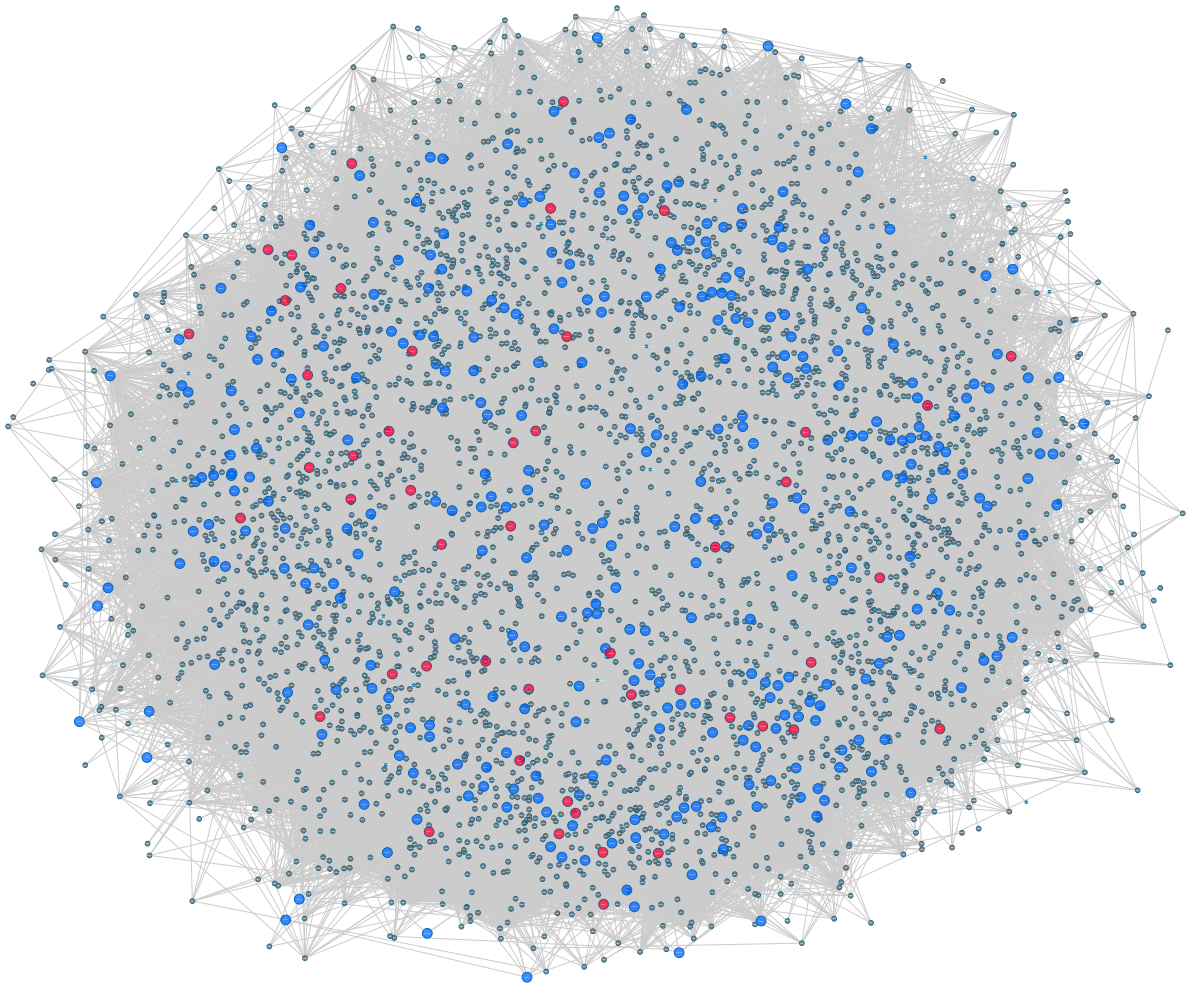
Non-cancerous endothelial cells contain podosomes that are closely related to invadopodia (Jacob and Prekeris, 2015). For OXS we detected significant decreases in nuclear abundance for SNAP23, VAMP3, STX12 and STX7 that are suggestive of changes in SNARE-related trafficking with the nucleus (Supplementary Table 2, preselected: filter = snare). VAMP7, VAT1 and VTI1B might be involved for OAC (Supplementary Table 1). For MMP14 such putative nuclear transfer via SNARE-related transport is mixed with more appreciable changes in total abundance. We did not detect SRC and EGFR in the nucleus, but there are other proteins such as ITGB1, basigin, Galectin-1 (LGAL1), Protein ERGIC-53 (LMAN1) and Utrophin (UTRN) that show little change in total abundance and closely parallel the strongly decreased nuclear abundance of SNAP23, VAMP3, STX7 and STX12 for OXS (Supplementary Table 2). All of them are known to have roles in ECM processes. We also detected many RAB proteins (RAB1A, RAB2A, RAB5A, RAB5C, RAB6A, RAB8A, RAB11B, RAB14) that closely paralleled the behaviour of SNAP23, VAMP3, STX12 and STX7 for OXS (Supplementary Table 2). RAB8 has previously been shown to be involved in delivery of MMP14 from a storage compartment to collagen contact sites (Bravo-Cordero et al., 2007). These results suggest that OXS changes what appear to be multiple vesicle-mediated processes for transferring proteins between the nuclear and cytoplasmic compartments. This could correspond to reduction of constitutive processes for transfer of proteins to the nucleus, to release of proteins from a (peri)-nuclear compartment, or to increasing evidence for involvement of endocytotic systems in mitotic processes. For example, RAB5 has been shown to contribute to lamin disassembly, chromosome alignment and transfer of NuMA to spindle poles (Capalbo et al., 2011) as well as to

chromosome congression and transfer of CENPB to kinetochores (Serio et al., 2011). Rab11 endosomes have been shown to be involved in spindle pole maturation and a number of other RABs, including RAB6, have been implicated in early mitosis (Das et al., 2014). The present results for RABs and MMP14 suggest further connections to endocytotic processes and the nuclear envelope/mitosis. Striking is that the changes in RAB proteins seem to be related to oxidative status (OXS) rather than suppression of DNA replication (OAC). These changes, and those for tetraspanins CD9 and CD63 (see below), might also be related to recent evidence for intricate involvement of vesicles enriched in endoplasmic components with the nuclear envelope in so-called “cytoplasmic capes” (Wu et al., 2014).

**Substantial changes for the tetraspanins CD9 and CD63 (OAC) are observed.** Tetraspanins are a large family of proteins expressed on the cell surface, in intracellular vesicles and in exosomes. The 33 tetraspanins identified in mammals have intricate involvement in proliferation, differentiation and immune response, and have been associated with a large variety of different cancers (Detchokul et al., 2014). Tetraspanins are involved in a multitude of biological processes that include cell adhesion, motility, invasion, or membrane fusion as well as signalling and protein trafficking and integrins are prominent among the proteins with which tetraspanins interact. A key feature is segregation into tetraspanin-enriched-microdomains (TEMs) that are distinct from lipid rafts or caveolae (Hemler, 2003, Yáñez-Mó et al., 2009). These domains are central for endosomal cycling and lead to a prominent role of tetraspanins in exosomes produced via multivesicular bodies (Andreu and Yáñez-Mó, 2014). We monitored three tetraspanins with high numbers of SILAC counts. CDC151 showed only modest SAME increases in total/cytoplasmic abundance (Supplementary Table 1). CD63 and CD9 were included in the 401-set. Both showed strong increase in cytoplasmic/total abundance for OAC only. Unexpectedly, C → N redistribution resulted in the strongest increase in abundance in the nuclear compartment ( $S_n = 3.76$ , 1.98 for CD63/CD9, Supplementary Table 2). Given that tetraspanins also modulate MMP14 trafficking (Schroder-2013) and given the cleavage of pericentrin-2 by MMP14 (Strongin, 2006), this suggests another axis for involvement of endocytotic trafficking with the cell cycle, one which is potentially independent of the endosomal sorting complex required for transport (ESCRTs) (Stuffers et al., 2009, Van Niel et al., 2011, Andreu and Yáñez-Mó, 2014).

**An appreciable reduction in the nuclear abundance of catenins CTNNA1, CTNNB1, and CTNND1 for OXS,** which are mostly a consequence of reduced total abundance (Supplementary Table 2), is another coordinated nuclear change of ECM-related proteins. These catenins are intimately involved both in cell junctions (cadherin complexes) and in transcriptional activities via many signalling pathways (McCrea et al., 2015, Klezovitch and Vasioukhin, 2015). Many of these pathways are also related to the epithelial-mesenchymal transition (EMT) or the closely related endothelial-mesenchymal (EndMT) transition that are prominent in both organ fibrosis and cancer progression/metastasis (Gonzalez and Medici, 2015). There is considerable and complicated overlap of the many signalling pathways, but in the present context the reduction of the nuclear abundance of catenins for OXS would appear to be a protective mechanism.

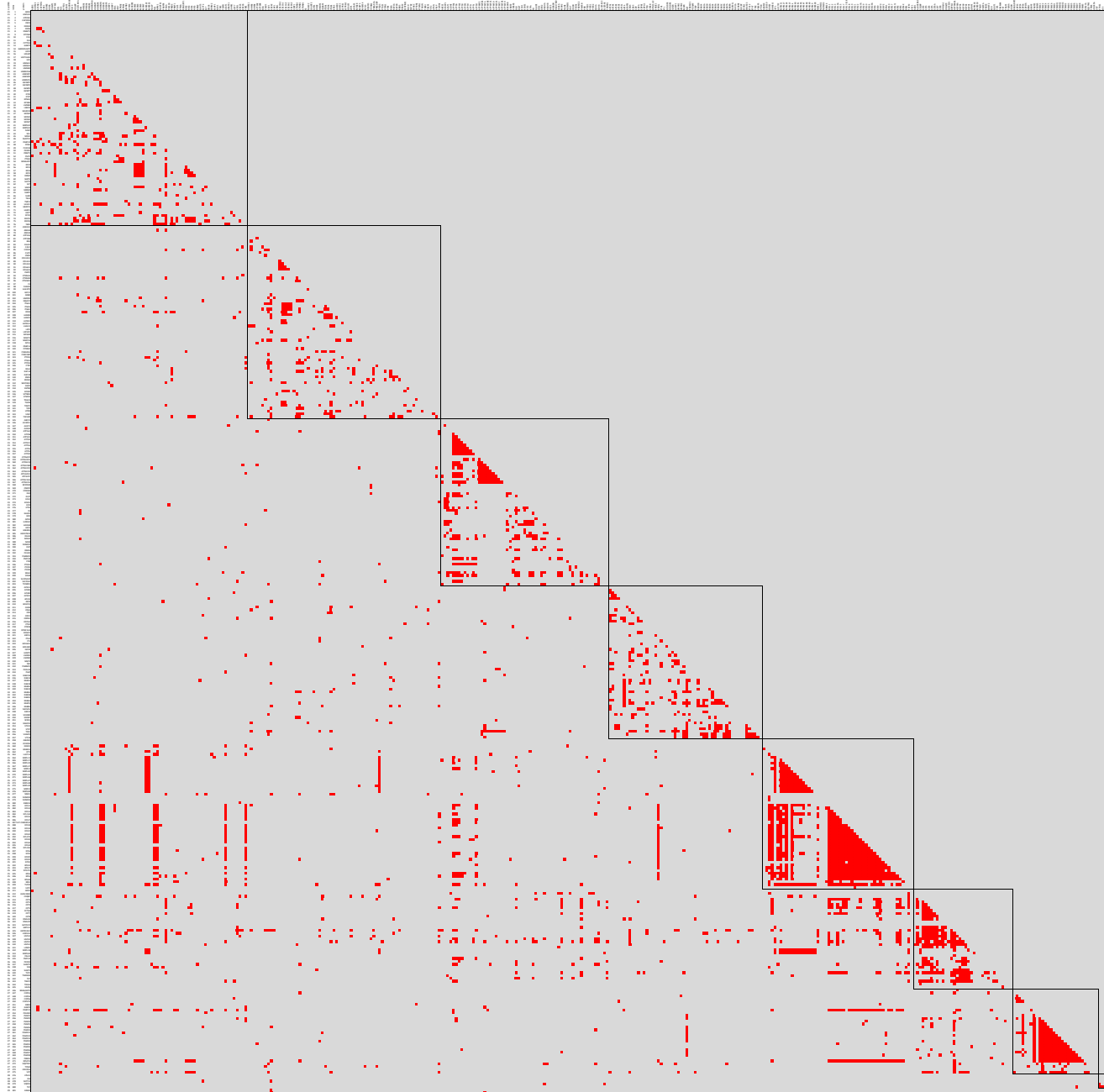
**References** (see Supplementary References)



Supplementary Figure 11. The overall set of 134,850 binary interaction pairs for the 4048-set of proteins. 49-set proteins are shown in red and 401-set proteins in blue. These latter proteins involve 3472 binary interactions (see main text). That is, although the overall network is enormously complex, a much smaller set of proteins and interactions seems to be adequate for coordination of spatially distributed responses across the cell.

Supplementary Figure 12. Interaction network for 401-set proteins clustered with the ClustNSee T-fit algorithm.

(A) Combined data set. 382 proteins, 3472 interactions.



**CLUSTER 1.** ADD3 ANP32E ATXN2L CAPRIN1 CBX1 DDX42 DDX6 DNMT1 DTYMK FIS1 FUS FYTDD1 G3BP1 GADD45GIP1 H1FX HDLBP HIST1H4A HK1 HMGAI HMG2 HMG8 HNRNPAB HNRNPF HNRNPK HNRNPU IGF2BP1 IGF2BP3 IGFBP5 IGFBP7 IPO5 IPO7 KPNA2 KPNB1 LMNB1 LSM12 MARCKS MCM2 MCM3 MCM5 MCM7 MRPS22 MRPS23 NASP NCL NPM1 NUDT21 PABPC4 PCNA PEX11B PRKDC PRMT1 PSIP1 PTMA RANGAP1 RFC2 RFC3 RFC4 RFC5 RRM2 SART3 SEPT2 SET SMC4 SRRM2 SSBP1 SUB1 TBL2 TMPO U2AF1 UBAP2L UHRF1 USP7 XPO1 XRCC5 XRCC6 YBX1

**CLUSTER 2.** ANXA11 ANXA2 ANXA4 ATP2A2 ATP2B4 BSG CALD1 CAV1 CDC42 CHP1 CNN1 COL12A1 COL1A1 COL1A2 COL6A1 COL6A2 CSRP1 CTNNA1 CTNNB1 CTNND1 F3 FAM3C GALNT2 GIPC1 GNB2 HMOX1 IQGAP1 ITGA1 ITGA5 ITGB1 KRAS LAMB1 LAMC1 LEPRE1 LEPREL1 LGALS1 LRP1 LRPAP1 MFG8 MGST3 MMP14 MYL3 OSBPL3 PITRM1 PRKAR1A PRKDCBP PTC3 PTCG1 PTPN1 PTRF RALA RAP1A RAP2B RND3 RRS2 SERPINE1 SGCD SNTB2 SPARC SPTBN1 STMN1 TAGLN TGFB1 TIMP1 TIP2 UTRN VASP YWHAZ

**CLUSTER 3.** ABCC1 ACADVL ACAT1 ALDH2 ATP5A1 ATP5B ATP5C1 ATP5D ATP5F1 ATP5H ATP5I ATP5L ATP5O ATP6A2 ATP6V0D1 ATP6V1A ATP6V1B2 ATP6V1C1 ATP6V1D ATP6V1E1 ATP6V1F ATP6V1G1 ATP6V1H BCKDHB CNDP2 CYB5R3 DLD DLST ECH1 ECHS1 EC12 ETFA FH GLUD1 GNS GPD2 HADHA HADHB HCCS HIBADH HSD17B10 IDH3A MDH2 NANS NOMO1 OAT OGDH P4HA1 PGRMC2 PMPCB POR PTCD1 PYCR1 PYCR2 SDHA SDHB SLC25A2 SLC25A3 TXNRD1

**CLUSTER 4.** AP2A1 AP2B1 AP3B1 AP3D1 AP3S1 ARF4 BCAP31 CANX CD63 CD9 COPA COPB1 COG1 CTSD CYB5B DYNC1L12 ERGIC1 ERO1L FTH1 FTL GOLGA3 GOLGB1 IGF2R LAMP1 LMAN1 LMAN2 M6PR NSF PGRMC1 PICALM PSAP RAB11B RAB14 RAB1A RAB1B RAB2A RAB34 RAB5A RAB5B RAB5C RAB6A RAB7A RAB8A SACM1L SAR1A SCARB2 SDCBP SFXN1 SNAP23 STX12 STX7 TERC VAMP3 VT11B

**CLUSTER 5.** ABLIM3 CCDC50 DDX21 GNB2L1 ICT1 LUC7L2 MRPL11 MRPL17 MRPL24 MRPL37 MRPL4 MRPL40 MRPL41 MRPL46 MRPL47 MRPL48 MRPL49 MRPL9 MRPS28 NME1 NOMO2 NOMO3 RBM14 RPL11 RPL12 RPL13 RPL13A RPL15 RPL17 RPL17-C18ORF32 RPL18 RPL19 RPL21 RPL22 RPL27A RPL29 RPL30 RPL34 RPL35A RPL6 RPL9 RPLP0 RPLP2 RPN1 RPS10 RPS17 RPS17L RPS2 RPS3 RPS4X RRS1 TUFM VAT1

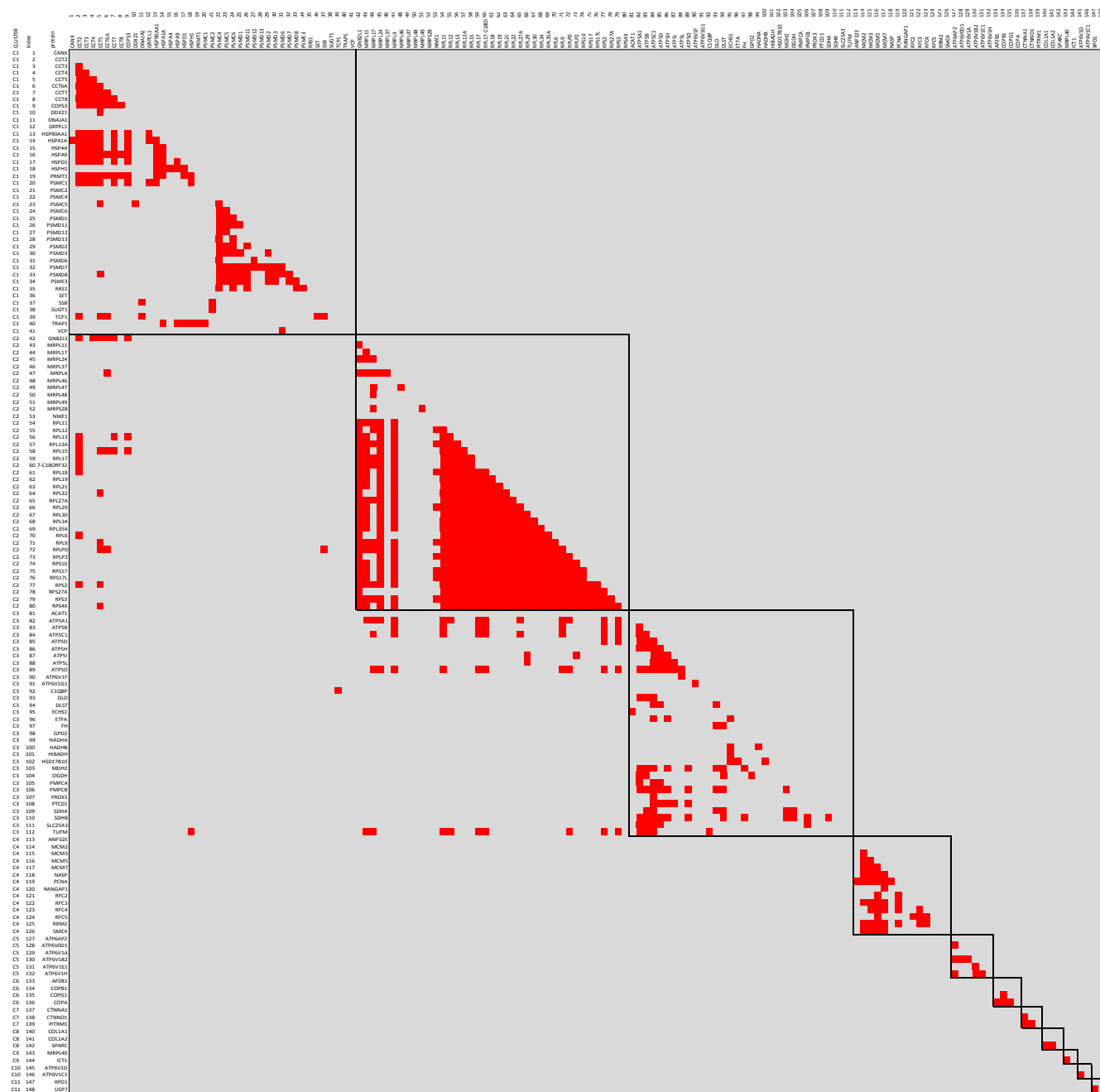
**CLUSTER 6.** ADD1 ALDH18A1 C1QB CT2 CT3 CT4 CT5 CT6A CT7 CT8 DNAJA1 DNAJC9 GLT25D1 GRPEL1 HSP90AA1 HSPA1A HSPA4 HSPA9 HSPD1 HSPH1 LONP1 MRPL18 MRPS30 PALLD PMPCA PRDX3 SHMT2 SSB SUGT1 TCP1 TIMM44 TKT TRAP1 TXLNA UGDH

**CLUSTER 7.** BAG6;BAT3 COPS3 COPS4 COPS6 COPS7A DBN1 G3BP2 PABPC1 PDLIM5 PSMC1 PSMC2 PSMC4 PSMC5 PSMC6 PSMD1 PSMD11 PSMD12 PSMD13 PSMD2 PSMD3 PSMD5 PSMD6 PSMD7 PSMD8 PSME3 RPS27A SQSTM1 TPM4 UNC45A VCP

**CLUSTER 8.** ETHE1 LSS SEPT11 SQRDL TST

**CLUSTER 9.** ARL8A ARL8B

Supplementary Figure 12. Interaction network for 401-set proteins clustered with the ClustNSee T-fit algorithm.  
 (B) Co-expression data set. 148 proteins, 906 interactions.



**CLUSTER 1.** CANX CCT2 CCT3 CCT4 CCT5 CCT6A CCT7 CCT8 COP35 DDX21 DNAJA1 GRPEL1 HSP90AA1 HSPA1A HSPA4 HSPA9 HSPD1 HSPH1 PRMT1 PSMC1 PSMC2 PSMC4 PSMC5 PSMC6 PSMD1 PSMD11 PSMD12 PSMD13 PSMD2 PSMD3 PSMD6 PSMD7 PSMD8 PSME3 RRS1 SET SSB SUGT1 TCP1 TRAP1 VCP

**CLUSTER 2.** GNB2L1 MRPL11 MRPL17 MRPL24 MRPL37 MRPL4 MRPL46 MRPL47 MRPL48 MRPL49 MRPS28 NME1 RPL11 RPL12 RPL13 RPL13A RPL15 RPL17 RPL17-C18ORF32 RPL18 RPL19 RPL21 RPL22 RPL27A RPL29 RPL30 RPL34 RPL35A RPL6 RPL9 RPLP0 RPLP2 RPS10 RPS17 RPS17L RPS2 RPS27A RPS3 RPS4X

**CLUSTER 3.** ACAT1 ATP5A1 ATP5B ATP5C1 ATP5D ATP5H ATP5I ATP5L ATP5O ATP6V1F ATP6V1G1 C1QBQ DLD DLST ECHS1 ETFA FH GPD2 HADHA HADHB HIBADH HSD17B10 MDH2 OGDH PMPCA PMPCB PRDX3 PTCD1 SDHA SDHB SLC25A3 TUFM

**CLUSTER 4.** ANP32E MCM2 MCM3 MCM5 MCM7 NASP PCNA RANGAP1 RFC2 RFC3 RFC4 RFC5 RRM2 SMC4

**CLUSTER 5.** ATP6AP2 ATP6V0D1 ATP6V1A ATP6V1B2 ATP6V1E1 ATP6V1H

**CLUSTER 6.** AP2B1 COPB1 COG1 COPA

**CLUSTER 7.** CTNNA1 CTNND1 PITRM1

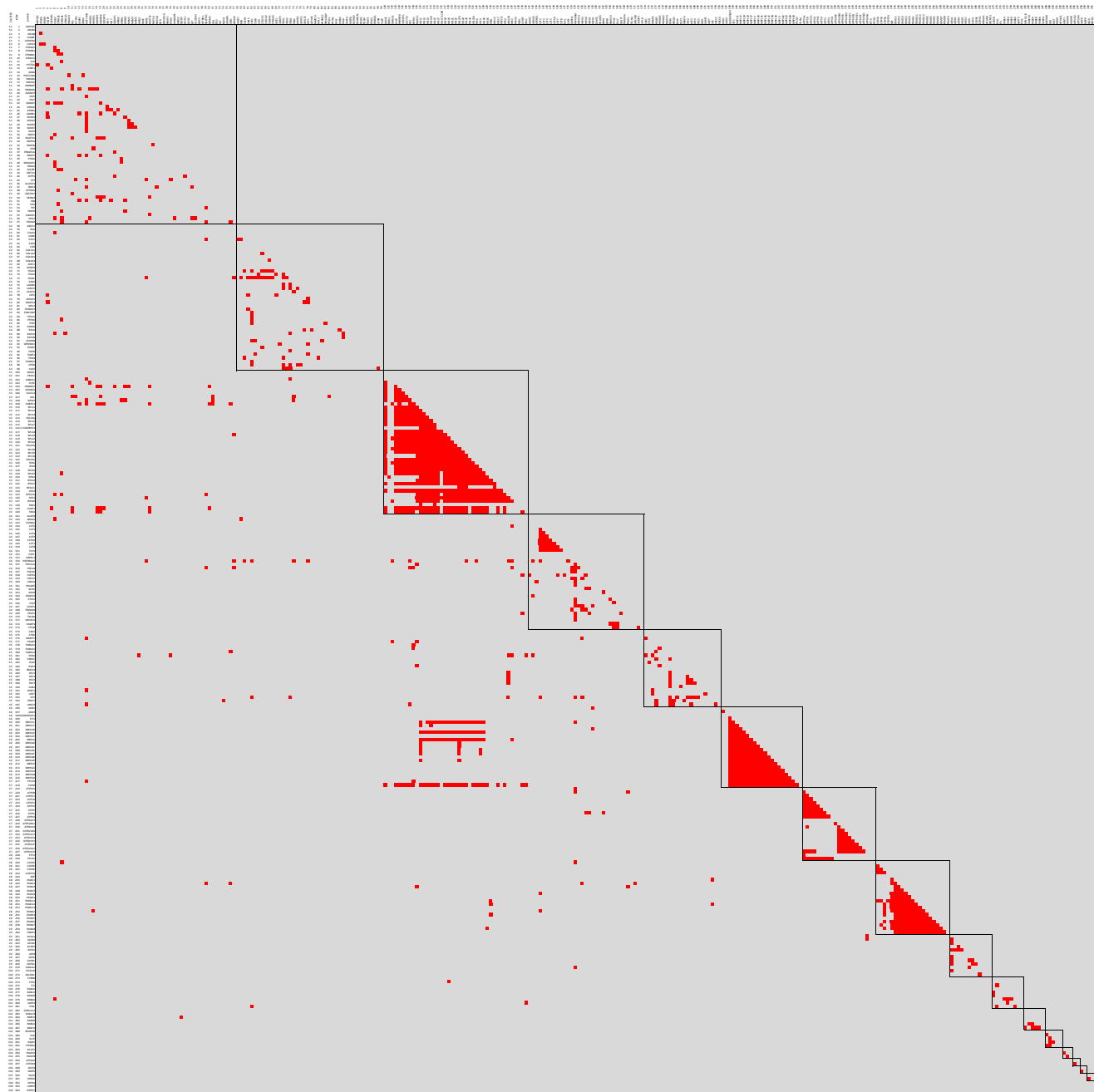
**CLUSTER 8.** COL1A1 COL1A2 SPARC

**CLUSTER 9.** MRPL40 ICT1

**CLUSTER 10.** ATP6V1D ATP6V1C1

**CLUSTER 11.** XPO1 USP7

Supplementary Figure 12. Interaction network for 401-set proteins clustered with the ClustNSee T-fit algorithm.  
 (C) Binding data set. 305 proteins, 1627 interactions.



**CLUSTER 1.** ANP32E ARL8A ARL8B C1QBP CAPRIN1 CDC42 CTNNA1 CTNNB1 CTNND1 DNAJC9 FUS FYTDD1 G3BP1 GNB2 HIST1H4A HMGB1 HMOX1 HNRNPF HNRNPK IGF2BP3 IPO5 IPO7 IQGAP1 KPNA2 KPNB1 LMNB1 MCM2 MCM3 MCM5 MCM7 NASP NME1 NUDT21 PMPCA PMPCB POR PRKAR1A PRMT1 PTMA RANGAP1 RRAS2 SDCBP SEPT11 SEPT2 SET SLC25A3 SMC4 SPTBN1 SQSTM1 SRRM2 SSB TJP2 TKT TMPO UBAP2L XPO1 YWHAZ

**CLUSTER 2.** ABCC1 BSG CALD1 CANX CAV1 CD63 CD9 COL1A1 COL1A2 COL6A1 COL6A2 GIPC1 IGFBP5 ITGA1 ITGA5 ITGB1 KRAS LAMB1 LAMC1 LGALS1 LRP1 LRPAP1 MMP14 MYL3 PGRMC1 PRKCDBP PTGS1 PTPN1 PTRF RAB34 RALA RAP1A RAP2B SCARB2 SERPINE1 SPARC TGFBI TIMP1 TPM4 TXNRD1 UTRN VASP

**CLUSTER 3.** DDX21 ERO1L GNB2L1 H1FX HNRNPU IGF2BP1 LUC7L2 NCL NPM1 PABPC1 RPL11 RPL12 RPL13 RPL13A RPL15 RPL17 RPL17-C18ORF32 RPL18 RPL19 RPL21 RPL22 RPL27A RPL29 RPL30 RPL34 RPL35A RPL6 RPL9 RPLPO RPLP2 RPN1 RPS10 RPS17 RPS17L RPS2 RPS27A RPS3 RPS4X RRS1 U2AF1 YBX1

**CLUSTER 4.** ALDH2 ANXA2 ATXN2L CCT2 CCT3 CCT4 CCT5 CCT6A CCT7 CCT8 TCP1 CHP1 GRPEL1 HSP90AA1 HSPA1A HSPA4 HSPA9 HSPD1 HSPH1 LSM12 PDLIM5 SDHA SDHB SNAP23 STX12 STX7 SUGT1 TIMM44 TRAP1 TXLNA UNC45A VAMP3 VT11B

**CLUSTER 5.** CBX1 CTSD DNMT1 HDLBP HMG1A HMG2 PABPC4 PCNA PRKDC PSAP PSIP1 RBM14 RFC2 RFC3 RFC4 RFC5 SUB1 UHRF1 USP7 VCP XRCC5 XRCC6

**CLUSTER 6.** ADD1 ADD3 GADD45GIP1 ICT1 MRPL11 MRPL17 MRPL18 MRPL24 MRPL37 MRPL4 MRPL40 MRPL41 MRPL46 MRPL47 MRPL48 MRPL49 MRPL9 MRPS22 MRPS23 MRPS28 MRPS30 PTCD3 TUFM

**CLUSTER 7.** ATP5A1 ATP5B ATP5C1 ATP5D ATP5F1 ATP5H ATP5I ATP5L ATP5O ATP6AP2 ATP6VOD1 ATP6V1A ATP6V1B2 ATP6V1C1 ATP6V1D ATP6V1E1 ATP6V1F ATP6V1G1 ATP6V1H ETFA PTCD1

**CLUSTER 8.** COPS3 COPS4 COPS6 COPS7A NSF PSMC1 PSMC2 PSMC4 PSMC5 PSMC6 PSMD1 PSMD11 PSMD12 PSMD13 PSMD2 PSMD3 PSMD5 PSMD6 PSMD7 PSMD8 PSME3

**CLUSTER 9.** AP2A1 AP2B1 AP3B1 AP3D1 AP3S1 ARF4 COPA COPB1 COPG1 DNAJA1 PICALM SACM1L

**CLUSTER 10.** CYB5B FTH1 FTL RAB14 RAB1A RAB1B RAB8A SART3 TFR3

**CLUSTER 11.** DYNC1L1 RAB11B RAB5A RAB5B RAB6A RAB7A

**CLUSTER 12.** BCKDHB DLD DLST OGDH PITRM1

**CLUSTER 13.** ACAT1 HADHA HADHB

**CLUSTER 15.** IGF2R M6PR

**CLUSTER 17.** IDH3A LONP1

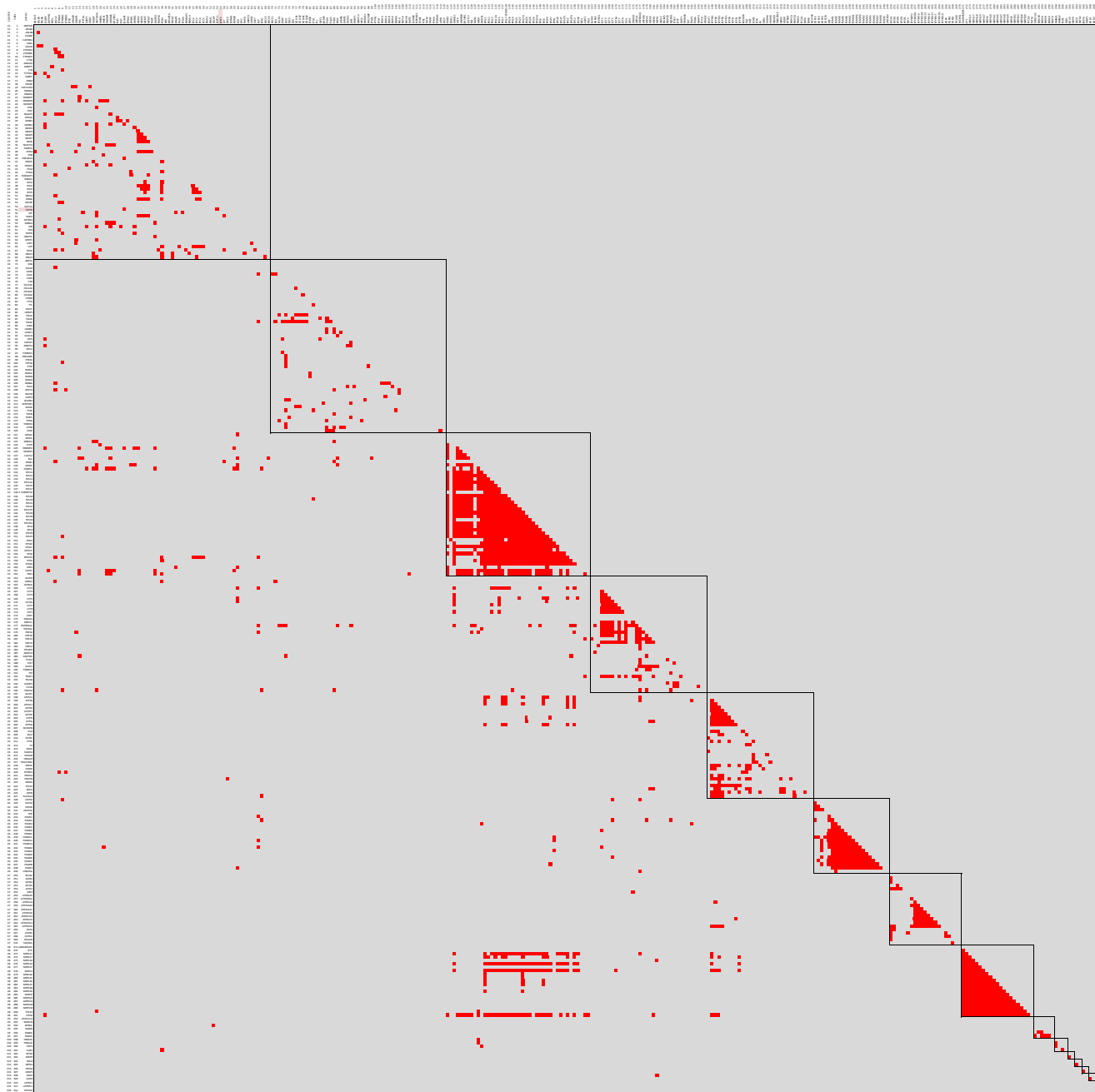
**CLUSTER 14.** ATP2A2 ATP2B4

**CLUSTER 16.** SGCD SNTB2

**CLUSTER 18.** LEPRE1 LEPREL1



Supplementary Figure 12. Interaction network for 401-set proteins clustered with the ClustNSee T-fit algorithm.  
 (D) Binding + co-expression data set. 313 proteins, 1964 interactions.



**CLUSTER 1.** ANP32E ARL8A ARL8B C1QBP CAPRIN1 CBX1 CDC42 CTNNA1 CTNNB1 CTNND1 CTSD DNAJC9 DNMT1 FUS FYTDD1 G3BP1 GNB2 HDLBP HIST1H4A HMGB1 HMOX1 HNRNPF HNRNPK IGF2BP3 IPO5 IPO7 IQGAP1 KPNA2 KPNB1 LMNB1 MCM2 MCM3 MCM5 MCM7 NASP NUDT21 PABPC4 PCNA POR PRKAR1A PRKDC PRMT1 PSAP PTMA RANGAP1 RBM14 RFC2 RFC3 RFC4 RFC5 RRAS2 RRM2 SDCBP SEPT11 SEPT2 SET SMC4 SPTBN1 SRRM2 SSB TJP2 TMPO UBAP2L UHRF1 USP7 VCP XPO1 XRCC5 XRCC6

**CLUSTER 2.** ABCC1 BSG CALD1 CANX CAV1 CD63 CD9 COL1A1 COL1A2 COL6A1 COL6A2 CYB5B FTH1 FTL GIPC1 IGFBP5 ITGA1 ITGA5 ITGB1 KRAS LAMB1 LAMC1 LGALS1 LRP1 LRPAP1 MMP14 MYL3 PGRMC1 PRKCD8P PTGS1 PTPN1 PTRF RAB14 RAB1A RAB1B RAB34 RAB8A RALA RAP1A RAP2B SART3 SCARB2 SERPINE1 SPARC TERC TGFB1 TIMP1 TPM4 TXNRD1 UTRN VASP

**CLUSTER 3.** DDX21 ERO1L GNB2L1 H1FX HNRNPU IGF2BP1 LUC7L2 NCL NME1 NPM1 PABPC1 RPL11 RPL12 RPL13 RPL13A RPL15 RPL17 RPL17-C18ORF32 RPL18 RPL19 RPL21 RPL22 RPL27A RPL29 RPL30 RPL34 RPL35A RPL6 RPL9 RPLP0 RPLP2 RPN1 RPS10 RPS17 RPS17L RPS2 RPS27A RPS3 RPS4X RRS1 U2AF1 YBX1

**CLUSTER 4.** ALDH2 ANXA2 ATXN2L CCT2 CCT3 CCT4 CCT5 CCT6A CCT7 CCT8 TCP1 CHP1 DNAJA1 GRPEL1 HSP90AA1 HSPA1A HSPA4 HSPA9 HSPD1 HSPH1 LSM12 PDLIM5 SNAP23 SQSTM1 STX12 STX7 SUGT1 TIMM44 TKT TRAP1 TXLNA VAMP3 VT1B YWHAZ

**CLUSTER 5.** ACAT1 ATP5A1 ATP5B ATP5C1 ATP5D ATP5F1 ATP5H ATP5I ATP5L ATP5O BCKDHB DLD DLST ECHS1 ETFA FH GPD2 HADHA HADHB HIBADH HSD17B10 MDH2 OGDH PITRM1 PMPCA PMPCB PRDX3 PTC1 SDHA SDHB SLC25A3

**CLUSTER 6.** COPS3 COPS4 COPS6 COPS7A NSF PSMC1 PSMC2 PSMC4 PSMC5 PSMC6 PSMD1 PSMD11 PSMD12 PSMD13 PSMD2 PSMD3 PSMD5 PSMD6 PSMD7 PSMD8 PSME3 UNC45A

**CLUSTER 7.** AP2A1 AP2B1 AP3B1 AP3D1 AP3S1 ARF4 ATP6A2 ATP6V0D1 ATP6V1A ATP6V1B2 ATP6V1C1 ATP6V1D ATP6V1E1 ATP6V1F ATP6V1G1 ATP6V1H COPA COPB1 COPG1 PICALM SACM1L

**CLUSTER 8.** GADD45GIP1 ICT1 MRPL11 MRPL17 MRPL18 MRPL24 MRPL37 MRPL4 MRPL40 MRPL41 MRPL46 MRPL47 MRPL48 MRPL49 MRPL9 MRPS22 MRPS23 MRPS28 MRPS30 PTC3 TUFM

**CLUSTER 9.** DYNC1L12 RAB11B RAB5A RAB5B RAB6A RAB7A

**CLUSTER 10.** HMG1 HMG2 PSIP1 SUB1

**CLUSTER 12.** SGCD SNTB2

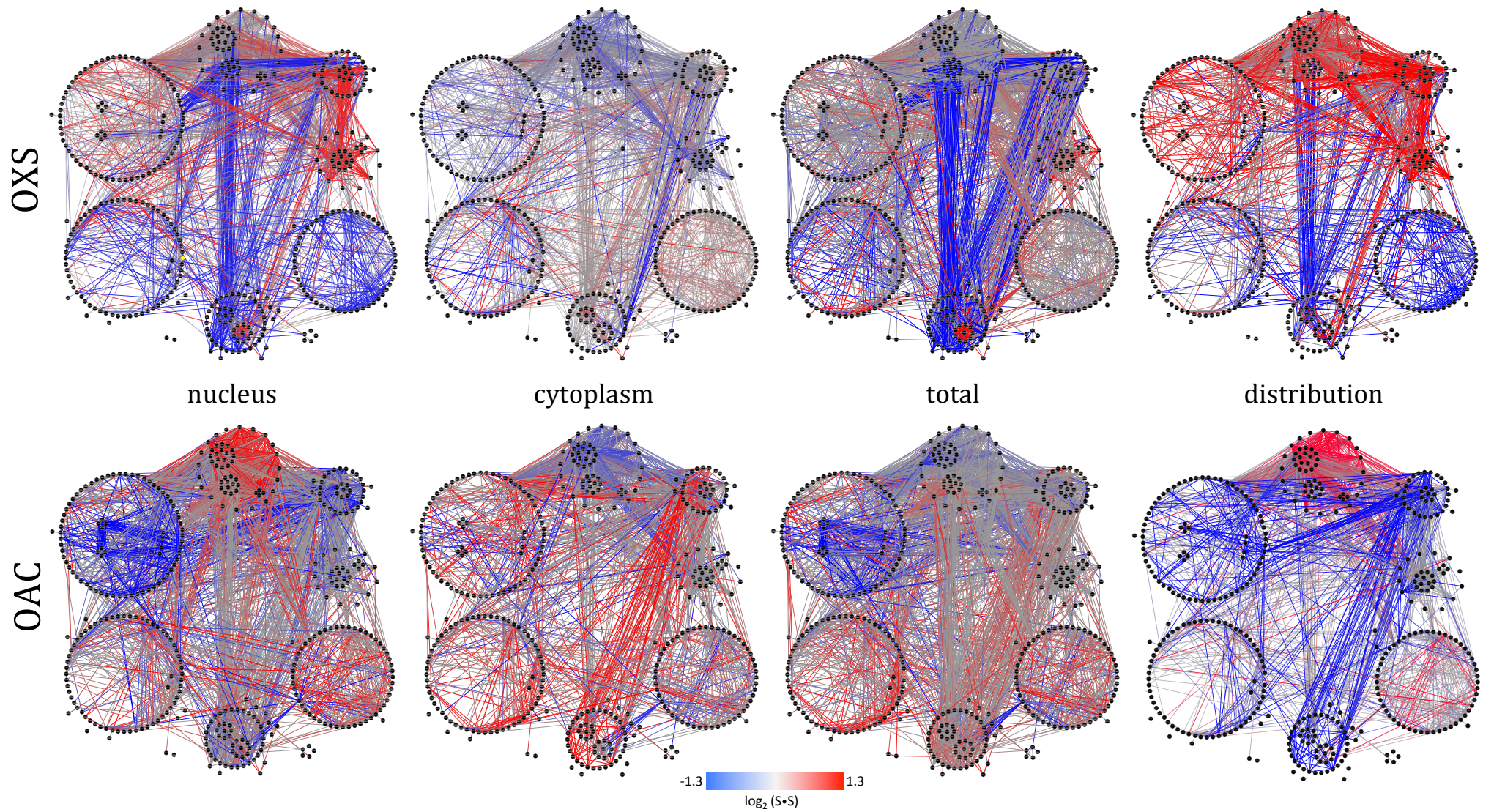
**CLUSTER 14.** ADD1 ADD3

**CLUSTER 16.** ATP2A2 ATP2B4

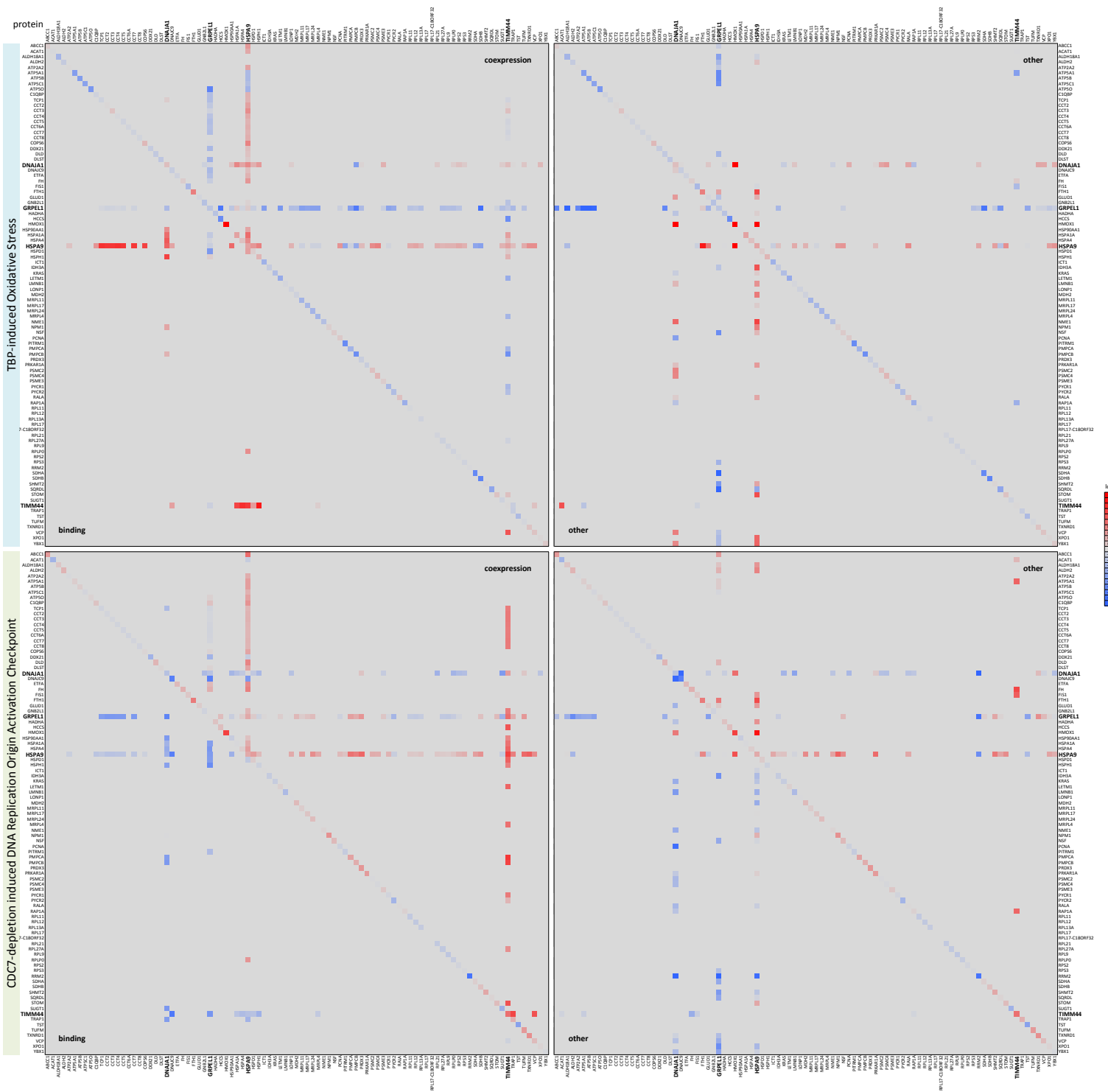
**CLUSTER 11.** IGF2R M6PR

**CLUSTER 13.** IDH3A LONP1

**CLUSTER 15.** LEPRE1 LEPREL1



Supplementary Figure 13. Experimental weighted interactions for the 401-set proteins for the clusters of the combined data set (Table 6). The edges are colored by  $\log_2(S^A * S^B)$  according to the scale.



Supplementary Figure 14. The local STRING-based interaction networks for OXS/OAC around the proteins DNAJA1, GRPEL1, HSPA9 and TIMM44. A set of 317 binary pair interactions was constructed by identifying a set of 89 additional 401-set proteins with interactions with at least two of the four seed proteins. The STRING interaction pairs were classified into three types as shown in the figure: (a) *co-expression*, (b) *binding*, and (c) *other* interaction pairs, the latter without (a) or (b) and many of which are largely based on text-mining or other experimental correlations. The experimental  $S_i$  data for each pair A-B was then mapped to the STRING *co-expression* pairs ( $S_t^A * S_t^B$ , upper off diagonal region) while the experimental  $S_n$  data was mapped to the STRING *binding* pairs ( $S_n^A * S_n^B$ , lower off diagonal region). The mechanism(s) underlying the correlation of the *other* pairs is often ambiguous and these pairs were therefore included symmetrically with mapping to  $S_t^A * S_t^B$  (upper off-diagonal region) and to  $S_n^A * S_n^B$  (lower off-diagonal region). Changes in total abundance for individual proteins ( $S_i$ ) were mapped to the diagonal.